

Special
Collection

Fast Charging Lithium Metal Batteries with Liquid and Solid-State Electrolytes

Kyobin Park,^[a] Juyeop Song,^[a] and Kyu Tae Lee^{*[a]}

The advent of fast charging technologies has revolutionized the field of energy storage, promising shorter charging times for lithium metal batteries. However, the pursuit of rapid charging capabilities presents several challenges, primarily due to the formation of lithium dendrites, which in turn, can lead to thermal runaway and safety risks. In this review, we first discuss the growth behavior of lithium metal in both liquid and solid-state electrolytes. Then, we outline the challenges and recent

progress in lithium metal batteries, particularly under fast charging conditions. Furthermore, we present comprehensive summary of the literatures on lithium metal batteries cycled at high current densities, investigating their performance with both liquid and solid-state electrolytes. Finally, we propose perspectives on various strategies aimed at addressing the challenges associated with lithium metal batteries under fast charging conditions.

1. Introduction

Fast charging in electric vehicles (EVs) alleviates range anxiety by facilitating rapid and convenient charging opportunities.^[1] EVs equipped with fast charging technology can offer refueling experiences comparable to internal combustion engine vehicles (ICEVs), effectively addressing concerns related to the limited driving range.^[2] However, current lithium-ion batteries (LIBs), comprising intercalation-type electrodes, such as layered transition metal oxide cathode materials and graphite anode materials, have reached a bottleneck with the theoretical energy density limits, and accordingly, the rechargeable batteries with new chemistry have become urgently required to improve energy density in our society.^[3] For this reason, lithium metal anodes (LMAs) have been considered a promising candidate for surpassing the energy density limits of current LIBs because the theoretical specific capacity and redox potential of lithium metal are 3860 mAh g⁻¹ and -3.04 V (vs. standard hydrogen electrode), respectively.^[4]

Fast charging in lithium metal batteries (LMBs) with liquid electrolytes (LEs) presents considerable challenges primarily due to the kinetics of plating/stripping processes, which differ from intercalation-type electrode materials.^[5] International organizations, including the International Standards Organization (ISO), the International Electrotechnical Commission (IEC), the Institute of Electrical and Electronics Engineers (IEEE), Society of Automotive Engineers (SAE), and Recommended National Standards of China (GB/T) established industry-wide standards for fast charging, which is 4 mA cm⁻² at a 1 C rate.^[6,7] Under such high current density of 4 mA cm⁻², the sluggish mass transport kinetics of lithium-ions give rise to concentration gradients between the bulk electrolyte and the LMA surface, resulting in inhomogeneous lithium deposition and dissolution.^[8] This contributes to the accelerated formation of lithium dendrites on the lithium metal surface, which exacerbates capacity fading and safety concerns.^[9] The increased lithium metal surface area resulting from dendritic growth of lithium metal promotes catastrophic electrolyte decomposition and continuous formation of a solid-electrolyte interphase (SEI)

due to the increased contact area between the highly reductive LMA and the electrolyte.^[10-11] Moreover, during repeated cycles, non-uniform, porous, and thick SEI layers accumulate on the lithium metal surface, hindering charge transfer kinetics, including lithium-ion diffusion through the SEI layers and lithium-ion desolvation at the SEI/electrolyte interface. This eventually engenders undesired lithium deposition morphology and inhomogeneity.^[12,13] Thus, regulating mass transport and charge transport kinetics in LEs for LMBs could pave the way for more reliable, efficient, and practical fast charging solutions, pushing the boundaries of energy storage technology.

Compared to LEs, solid electrolytes (SEs), such as Li₆PS₅Cl (LPSCl), Li₁₀GeP₂S₁₂ (LGPS), and Li₂La₃Zr₂O₁₂ (LLZO), offer several theoretical advantages owing to their high lithium-ion transference number ($t_{Li^+} \approx 1.0$), rigid mechanical property, and enhanced safety, which can potentially address challenges associated with dendritic growth of lithium metal under fast charging conditions.^[14,15] Moreover, all-solid-state lithium metal batteries (ASSLMBs) have the potential to enable exceptionally high volumetric energy density (>1100 Wh L⁻¹), which is far beyond LIBs (≈ 700 Wh L⁻¹) and LMBs with LEs (≈ 900 Wh L⁻¹).^[16,17] Despite their theoretical benefits, we are concerned about ASSLMBs because many other critical factors play a decisive role in influencing the dendritic growth of lithium metal during fast charging. For example, the presence of grain boundaries, defects, and surface roughness between the SE/LMA interface can serve as nucleation sites for dendrite initiation.^[18-19] Cell volume changes during lithium plating/stripping can also give rise to mechanical stresses on the SE, inducing deformation and cracking of the solid electrolyte, which can promote dendrite initiation and propagation.^[20,21] Moreover, since these issues are entangled with each other, a fundamental understanding of the lithium dendrite growth mechanism in SEs is essential to improve the fast charging capability of ASSLMBs. In this review, we underline recent progress in LMBs with liquid and solid electrolytes, specifically under fast charging conditions. We also demonstrate the growth mechanism of lithium metal in both liquid and solid-state electrolytes. Finally, we present future perspectives and limitations of each strategy to address the challenges associated with fast charging conditions.

[a] K. Park, J. Song, Prof. K. T. Lee

School of Chemical and Biological Engineering,
Institute of Chemical Processes,
Seoul National University
1 Gwanak-ro, Gwanak-gu, Seoul
08826 (Republic of Korea)
E-mail: ktlee@snu.ac.kr

 An invited contribution to a Special Collection on Fast Charging Batteries

2. Fast Charging in Lithium Metal Batteries with Liquid Electrolytes

Efficient electrolyte mass transport is vital for maintaining a homogeneous distribution of lithium-ion flux, thereby mitigating the localized depletion of lithium-ions and inhibiting dendritic growth. The onset time for dendrite initiation can be rationally described by the Sand's equation [Equation (1)], in which the lithium-ion concentration reaches zero at the lithium metal surface under diffusion limiting condition.^[22]

$$\tau = \frac{(zC_0F)^2}{\pi D_{Li^+} 4J^2(1 - t_{Li^+})^2} \quad (1)$$

In the equation, τ , D_{Li^+} , z , C_0 , F , J , and t_{Li^+} are the Sand's time, the diffusion coefficient of lithium-ion, electronic charge, bulk concentration of the electrolyte, Faraday's constant, current density, and transference number of lithium cations, respectively. LEs generally have a transference number of lithium cations about 0.2 to 0.3.^[23,24] According to the equation, the concentration polarization undergoes significant variation at higher current densities, resulting in the depletion of lithium-ions and the decrease in ionic conductivity near the lithium metal surface. For this reason, lithium dendrite growth is accelerated particularly under fast charging condition, hindering practical application of LMBs. However, mass transport limiting in the bulk electrolyte is not the only factor determining lithium dendrite growth, and thus, many other factors should be considered, such as lithium-ion transport kinetics through the SEI, lithium-ion desolvation kinetics, and the uniformity and stability of the SEI layers (Figure 1).^[25,26] In this

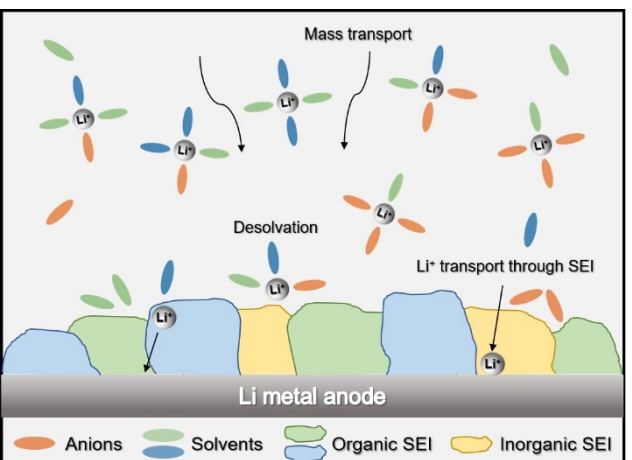


Figure 1. Schematic illustration of mass transport for the electroplating process of lithium metal with liquid electrolytes.

section, recent progress and strategies to address the above issues are thoroughly discussed.

2.1. Regulating bulk electrolyte pathways

Electric double layer (EDL) refers to the interface between the electrode and the electrolyte, where the inner Helmholtz plane (IHP) and the outer Helmholtz plane (OHP) establish charge neutrality.^[27,28] In LMBs, IHP is generally formed through the selective adsorption of anions on the electrode surface, and solvated lithium cations are attracted towards the negatively charged IHP for counterbalance, resulting in the formation of



Kyu Tae Lee is currently a professor in the School of Chemical and Biological Engineering at Seoul National University. He received his Ph.D. at Seoul National University in 2006, after which he conducted his post-doctoral research at University of Waterloo from 2007 to 2010. He began to conduct independent research at Ulsan National Institute of Science and Technology (UNIST) since 2010 until he moved to Seoul National University in 2015. His research interests span from the fundamental understanding of electrochemistry to the development of new electrochemical systems for energy storage and conversion devices, with a focus on practical applications.



Juyeop Song is currently a PhD student in School of Chemical and Biological Engineering at Seoul National University. He obtained his bachelor's degree in chemical and biological engineering from Seoul National University in 2021. His research interests include developing strategies for fast charge applications in all-solid-state lithium metal batteries, as well as understanding electrochemical mechanisms of anode in anode-free solid-state lithium batteries.



Kyobin Park is currently a PhD student in School of Chemical and Biological Engineering at Seoul National University. He obtained his bachelor's degree in chemical and biological engineering from Korea University in 2019. His current research interests lie with designing electrolytes and material characterization for lithium metal batteries, with a focus on exploring their electrochemical mechanism.

OHP.^[29,30] When the selective adsorption of anions increases in the IHP, not only does the t_{Li^+} increase, but also more lithium-ions are attracted to the OHP, sufficiently supplying lithium-ions to the lithium metal surface. In this regard, the regulation of electrolyte transport pathways through the construction of porous nanostructures on the lithium metal electrode emerges as a promising strategy. The surface of the porous medium is known to form an EDL during charging, which facilitates the mass transport properties of the bulk electrolytes, including ionic conductivity and t_{Li^+} .^[31,32]

Hao et al. introduced an electronegative nanochannel separator to induce the formation of EDL at the surface of the porous medium, by applying a polyacrylic acid (PAA) solution to the porous anodic aluminum oxide (AAO) membrane using an osmosis process (Figure 2a).^[33] The EDL formed on the inner surface of the electronegative nanochannel contributed to the fast conduction of lithium-ions, demonstrating high lithium cation selectivity ($t_{\text{Li}^+} = 0.77$) and conductivity (1.36 mS cm^{-1}) compared to commercial separators. As a result, the Li | Li symmetric cell exhibited stable cycling for 2000 hours at a high current density of 5 mA cm^{-2} with an areal capacity of 2.5 mAh cm^{-2} . Guo et al. incorporated thermally conductive aluminum nitride (AlN) nanowires into a commercial polypropylene (PP) separator to mitigate localized thermal hotspots that occur during dendritic growth of lithium metal (Figure 2b).^[34] The AlN-PP composite separator was prepared using a vacuum filtration process. The high thermal conductivity of the AlN nanowires ($319 \text{ W m}^{-1} \text{ K}^{-1}$) effectively dissipated potential thermal gradient across the separator, thereby regulating homogeneous lithium deposition. Furthermore, the electrolyte-philic and robust properties of the AlN network improved lithium-ion diffusion kinetics and provided mechanical strength to suppress dendrite formation, respectively. The Li | Li symmetric cell demonstrated stable cycling over 1000 hours at a high current density of 80 mA cm^{-2} with an areal capacity of 80 mAh cm^{-2} . Jung et al. fabricated a porous aramid nanofiber (PANF) separator with high porosity ($> 97\%$) by controlling the reprotoonation process through a two-step solvent exchange method: immersion in ethanol followed by deionized (DI) water (Figure 2c).^[35] Highly porous structure of PANF with amide groups, which have a high affinity towards PF_6^- anions, significantly contributed to the increased ionic conductivity of 1.87 mS cm^{-1} and t_{Li^+} of 0.84. Eventually, the PANF separator showed stable cycle performance of Li | LFP full cell, such as a capacity retention of 86.3% after 1000 cycles, even at a high charging rate of 30 C.

Most batteries rely on diffusion to replenish lithium-ions on the electrode surface. However, the 100 MHz surface acoustic wave (SAW) device introduced by Huang et al., which induces forced flow to the electrolyte, promotes lithium-ion migration, significantly reducing concentration gradients in the electrolyte (Figure 2d).^[36] Moreover, this fingernail-sized device, widely used in small microfluidics applications, can generate a fluid flow of up to 1 m s^{-1} . The porosity of the deposited lithium with the SAW device was 19%, whereas that without the SAW device was 82%, indicating dense and non-dendritic growth of lithium metal during forced electrolyte flow at a high current density of

6 mA cm^{-2} . Additionally, the rate performance of the Li | LFP full cell showed a five-fold increase in discharge capacity (55 mAh g^{-1}) at 6 mA cm^{-2} with the SAW device.

However, while fast charging characteristics can be improved by regulating mass transport properties of the electrolytes, it is inevitable that this strategy will experience a loss of energy density due to an increase in the weight of cell materials, such as modifications of the separator and the adoption of new device. Therefore, it is important to recognize that a tradeoff relationship exists between fast charging and energy density.

2.2. Regulating homogeneous lithium-ion flux

Mass transport property of lithium-ions can also be improved through the modification of the electrode/electrolyte interface.^[37] The presence of a well-engineered artificial SEI layer, designed to function as a lithiophilic site, a lithium-ion transport channel, and a lithium nucleation site, facilitates a homogeneous lithium-ion flux, thereby effectively mitigating local plating and stripping, particularly under fast charging conditions.

Cao et al. employed a low-tortuous MXene (TiNbC-MXene) accordion array layer as an artificial SEI in LMBs using a super-spreading technique (Figure 3a).^[38] When an aqueous solution containing dispersed MXene was applied at the water/methylene chloride interface, the strong driving force of surface tension and gravity induced the dispersed phase to spread into a thin layer. Once the TiNbC-MXene film was applied to a Cu current collector for anode-free cell application, the electrode exhibited excellent wetting properties against the electrolyte due to the low tortuosity of the MXene, thereby improving lithium-ion transport properties. The accordion array layer also contributed to the uniform nucleation of lithium metal plating. Moreover, the Nb species of MXene enhanced charge transfer kinetics, further contributing to the homogenization of the electric field distribution. TiNbC-MXene-Li electrode was prepared by depositing 6 mAh cm^{-2} of lithium onto the TiNbC-MXene substrate. The TiNbC-MXene-Li | TiNbC-MXene-Li symmetric cell demonstrated stable cycling for 200 hours at a high current density of 20 mA cm^{-2} and the TiNbC-MXene-Li | LFP full cell also showed stable capacity retention (86%) for 1000 cycles at a 4 C rate (Figure 3b). Ye et al. introduced a lithium-ion adsorbing layer (LAL).^[39] The LAL/Li | LAL/Li symmetric cell demonstrated long-term cycle stability over 1000 hours, even at a high current density of 60 mA cm^{-2} and an areal capacity of 60 mAh cm^{-2} (Figure 3c). The LAL layer was fabricated by spin-casting a sulfoxide/acetonitrile solution containing dispersed graphene quantum dots onto the lithium metal anode (Figure 3d). The LAL exhibited a strong lithium-ion affinity driven by the electronegative characteristics of the graphene quantum dot surface, including $-\text{OH}$, $-\text{COOH}$, $\text{C}=\text{O}$, and $-\text{O}, \text{N}, \text{S}$ containing groups. As a result, the LAL provided spatial confinement of lithium-ion flux at the electrode surface ($t_{\text{Li}^+} = 0.57$). Additionally, the high modulus of graphene (6.22 GPa) contributed to suppressing lithium dendrite growth within the LAL/Li.

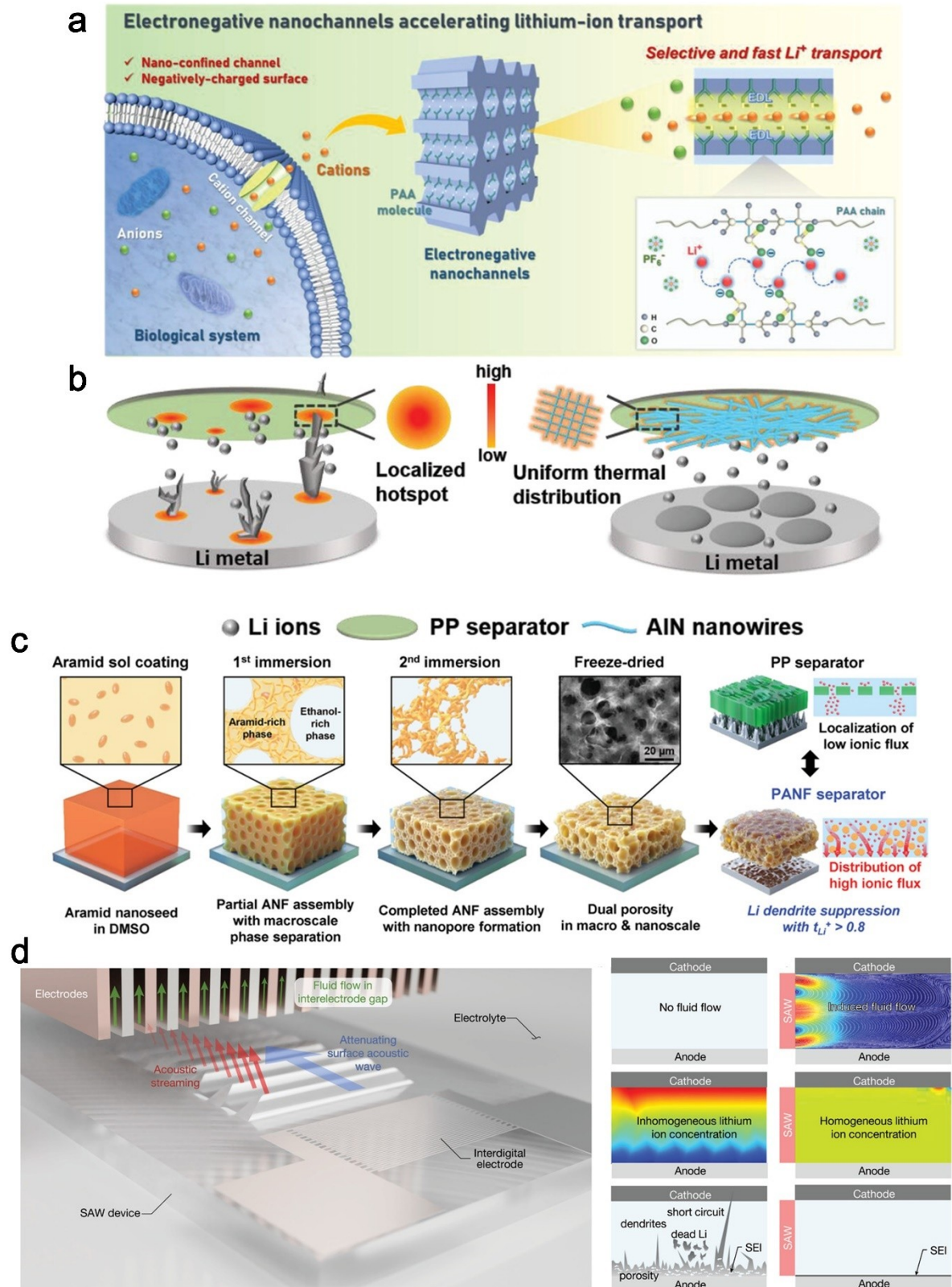


Figure 2. a) Accelerated lithium-ion transport kinetics inside the porous nanochannels. Reproduced from ref. [33] Copyright (2023), with permission from Wiley-VCH. b) Uniform lithium deposition behavior in the AlN-PP composite separator compared to the pristine PP separator. Reproduced from ref. [34] Copyright (2022), with permission from Wiley-VCH. c) Fabrication process of porous aramid nanofiber (PANF) separator through two-step solvent exchange method. Reproduced from ref. [35] Copyright (2022), with permission from Wiley-VCH. d) Accelerated lithium-ion transport kinetics by forced electrolyte flow using surface acoustic wave (SAW) device. Reproduced from ref. [36] Copyright (2020), with permission from Wiley-VCH.

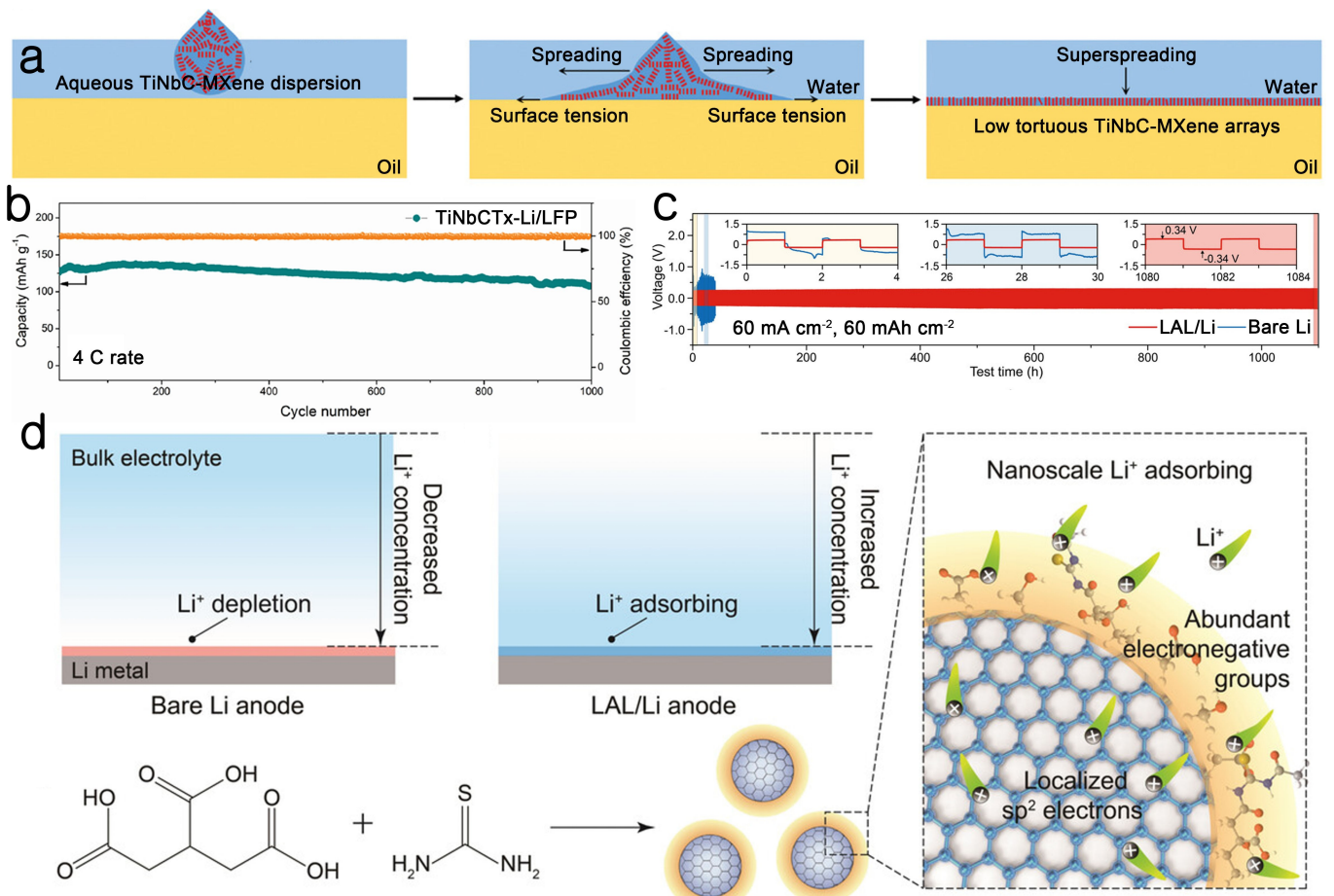


Figure 3. a) Fabrication process of a low-tortuous MXene (TiNbC-MXene) accordion array layer using a super-spreading technique. b) Cycle performance of TiNbC-MXene-Li | LFP full cell at a 4 C rate. Reproduced from ref. [38] Copyright (2022), with permission from Wiley-VCH. c) Cycle performance of LAL/Li | LAL/Li symmetric cell at a current density of 60 mA cm^{-2} and an areal capacity of 60 mAh cm^{-2} . d) Increased lithium-ion flux with lithium-ion adsorbing layer (LAL) compared to bare Li. Reproduced from ref. [39] Copyright (2021), with permission from Wiley-VCH.

Hu et al. proposed an artificial hybrid SEI composed of LiF and Li₃Sb by immersing lithium metal electrode in a SbF₃-containing 1,2-dimethoxyethane (DME) solution at room temperature.^[40] Owing to the superior diffusion coefficient of Li₃Sb ($2.0 \times 10^{-4} \text{ cm}^2 \text{s}^{-1}$), the Li₃Sb (110) surface showed a lower lithium-ion diffusion energy barrier of 0.09 eV compared to 0.28 eV for LiF (001) and 0.39 eV for Li (001). Moreover, LiF is known to effectively block electrons from tunneling effect, due to its low electronic conductivity.^[41,42] The authors also elucidated the lithium-ion transport mechanism of the artificial hybrid SEI by comparing the electrostatic potential of the hybrid SEI with that of a common SEI using finite element simulation. This comparison helped in understanding the dynamic changes of diffusion kinetics within the multi-component SEI structure. Consequently, the synergistic effect of the LiF/Li₃Sb hybrid SEI layer allowed stable cycling of the Li | Li symmetric cell over 300 hours at a high current density of 20 mA cm^{-2} and an areal capacity of 2 mAh cm^{-2} . Wu et al. also fabricated a thin Fe/LiF nanocomposite layer to regulate the initial nucleation and growth morphology of lithium metal.^[43] The Fe/LiF layer was prepared by thermally evaporating FeF₃ onto a Cu current collector followed by in-situ reaction with

lithium metal, where nanosized Fe particles were uniformly and extensively spread, providing uniform lithium nucleation sites. Lithium metal deposited on the Fe/LiF layer showed hexagonal-shaped single-crystalline lithium terminated with low energy (110) facet even at a high current density of 5 mA cm^{-2} , which was confirmed by cryo-TEM analysis. This unique deposition morphology was attributed to the high surface diffusion of LiF, leading to thermodynamically stable morphology.^[44,45] Moreover, it was emphasized that the interfacial diffusion kinetics was more critical than the lithiophilicity of the substrate for achieving uniform deposition of lithium metal, because the presence of the Fe/LiF layer improved electrodeposition uniformity, despite Cu metal being a lithiophobic substrate. As a result, Fe/LiF-Cu | Li cell successfully operated at a high current density of 5 mA cm^{-2} and an areal capacity of 3 mAh cm^{-2} for 600 cycles.

Although artificial SEI layers offer a relatively straightforward process to enhance lithium-ion transport properties at the electrode/electrolyte interface, it is notable that its recovery becomes challenging if the coating layer is unstable and deformed during cycling.

2.3. Modification of electrode structure

Current density significantly influences the deposition morphologies of lithium metal. At high current density, the rapid depletion of lithium-ions on the electrode surface outpaces their reduction, leading to the formation of whisker-like lithium metal structures.^[46–48] This behavior aligns with the Sand's equation [Equation (1)], where the square of current density is inversely proportional to the dendrite onset time (Sand's time) implying that higher current density accelerates lithium dendrite growth. Furthermore, the chemical composition of the SEI layer is highly sensitive to current density, affecting its mechanical strength, ionic conductivity, and overall stability. For example, Xu et al. observed a monolithic amorphous SEI at a low current density (0.1 mA cm^{-2}), while a mosaic nanostructured SEI composed of Li_2O and LiF matrix was observed at a high current density ($>2 \text{ mA cm}^{-2}$) using a 1.2 M lithium hexafluorophosphate (LiPF_6) in ethylene carbonate/ethyl methyl carbonate (EC/EMC) electrolyte.^[49] Considering these factors, modified 3D porous frameworks offer notable advantages over conventional 2D lithium metal electrodes because 3D porous frameworks with high surface area reduces areal current density compared to 2D substrates. The increased surface area of these 3D frameworks plays a crucial role in reducing the local current density, effectively confining lithium metal within the pores, and ultimately facilitating a more uniform and controlled lithium plating process.^[50–52]

The surface functionality and structure of the pore are also critical factors that affect uniform deposition of lithium inside the 3D framework. Choi et al. demonstrated the role of surface craters in regulating the uniform lithium storage by comparing SiO_2 surface functioned porous carbon framework (SC-PCF) with pristine PCF.^[53] MacMullin number (N_M), which is the parameter representing the ratio of the bulk electrolyte ionic conductivity to the effective ionic conductivity of the electrolyte confined in porous structure, was estimated using AC-impedance (Figure 4a). SC-PCF showed higher N_M than that of PCF, suggesting facile lithium-ion transport inside the surface-functionalized porous structure. Gong et al. designed a 3D structured carbon host capable of accommodating its capacity through both intercalation and plating of lithium-ions.^[54] In contrast to the sphere-shaped hard carbon, which is known for sluggish internal diffusion, the flower-like hard carbon architecture (CF) demonstrated enhanced lithium-ion diffusion kinetics, which was attributed to its unique open-pore structure. The open-pore nanostructure also provided additional sites for the uniform confinement of lithium plating. As a result, the $\text{Li}|\text{NCM}811$ full cell (2 mAh cm^{-2}) exhibited promising cycle performance over 200 cycles at a high current density of 10 mA cm^{-2} .

However, at high current densities, the top plating of lithium metal is observed for 3D porous frameworks because the ionic resistance of electrolytes in the porous structure significantly increases with increasing distance from the top surface. To address this issue, Song et al. fabricated Au nano-seed-embedded 3D structure in the carbonized cellulose and CNT foam (Au/CCC).^[55] Carbothermal shock method (CTS) was

used to reduce Au precursor to Au nanoparticles (NPs) and carbonize cellulose to defective carbon at 1450 K. The presence of defective carbon in the carbon support offered numerous anchoring sites for the Au NPs, leading to the uniformly embedded dispersion of Au NPs. Lithiophilic Au NPs further contributed to the uniform deposition of lithium metal inside the 3D CNT structure. As a result, the $\text{Au/CCC}|\text{Li}$ cell exhibited excellent cycle performance over 200 cycles at a current density of 5 mA cm^{-2} and an areal capacity of 3 mAh cm^{-2} . Kang et al. adopted core-shell type porous hollow carbon fibers with an interior Au coating (Au@PHCF) as a material for the 3D host (Figure 4b).^[56] In addition to the advantages of the general 3D framework, the presence of an additional porous structure facilitated easier lithium-ion transport, with the lithiophilic Au coating providing nucleation sites. Consequently, the $\text{Au@PHCF-Li}|\text{LFP}$ full cell demonstrated stable cycling performance, sustaining over 500 cycles at a 4 C rate. Similarly, Fang et al. fabricated Ag nanoparticle-embedded, nitrogen-doped carbon microporous fibers as a 3D lithium host (Figure 4c).^[57] The lithiophilic properties of Ag nanoparticles and nitrogen-doped carbon sites enabled lithium deposition to exhibit small voltage hysteresis, which was demonstrated by the rate performance test at various current densities (0.5, 1, 2, 3, 5, 10, 20, and 30 mA cm^{-2}) with a fixed areal capacity of 2 mAh cm^{-2} . The $\text{Li}|\text{Li}$ symmetric cell showed a stable cycling over 300 hours at a high current density of 10 mA cm^{-2} . Park et al. proposed a 3D porous Li–Si alloy-type interfacial framework (LSIF) formed by an in-situ prelithiation reaction (Figure 4d).^[58] After the cell was assembled with an ultrathin n-type Si wafer on a lithium foil, a robust ion/electron conducting 3D framework (LSIF@Li), consisting of lithiophilic $\text{Li}_{15}\text{Si}_4$, was spontaneously formed by a self-discharge reaction. This unique structure exhibited high lithium-ion affinity, fast diffusion kinetics, and low nucleation barriers. As a result, the $\text{LSIF@Li}|\text{LSIF@Li}$ symmetric cell managed to operate at a high current density of 15 mA cm^{-2} for over 1000 cycles. In addition, the $\text{LSIF@Li}|\text{NCM}523$ full cell showed superior cycling stability over 1000 cycles at a 10 C rate.

It is definite that 3D structured frameworks reduce the effective current density, thereby improving the rate performance. However, the additional volume and weight of the 3D frameworks decrease in the volumetric and gravimetric energy densities, respectively. Besides, the porous structure of the framework gives rise to a significant increase in electrolyte resistance along the depth direction. As a result, the overall resistance, including charge transfer and mass transfer resistances, of the 3D frameworks is not uniform along the depth direction, thereby inducing the “top plating” of the 3D frameworks. Therefore, it is demanded to control overall resistance uniformly along the depth direction of the 3D frameworks to obtain the superconformal plating of lithium metal.

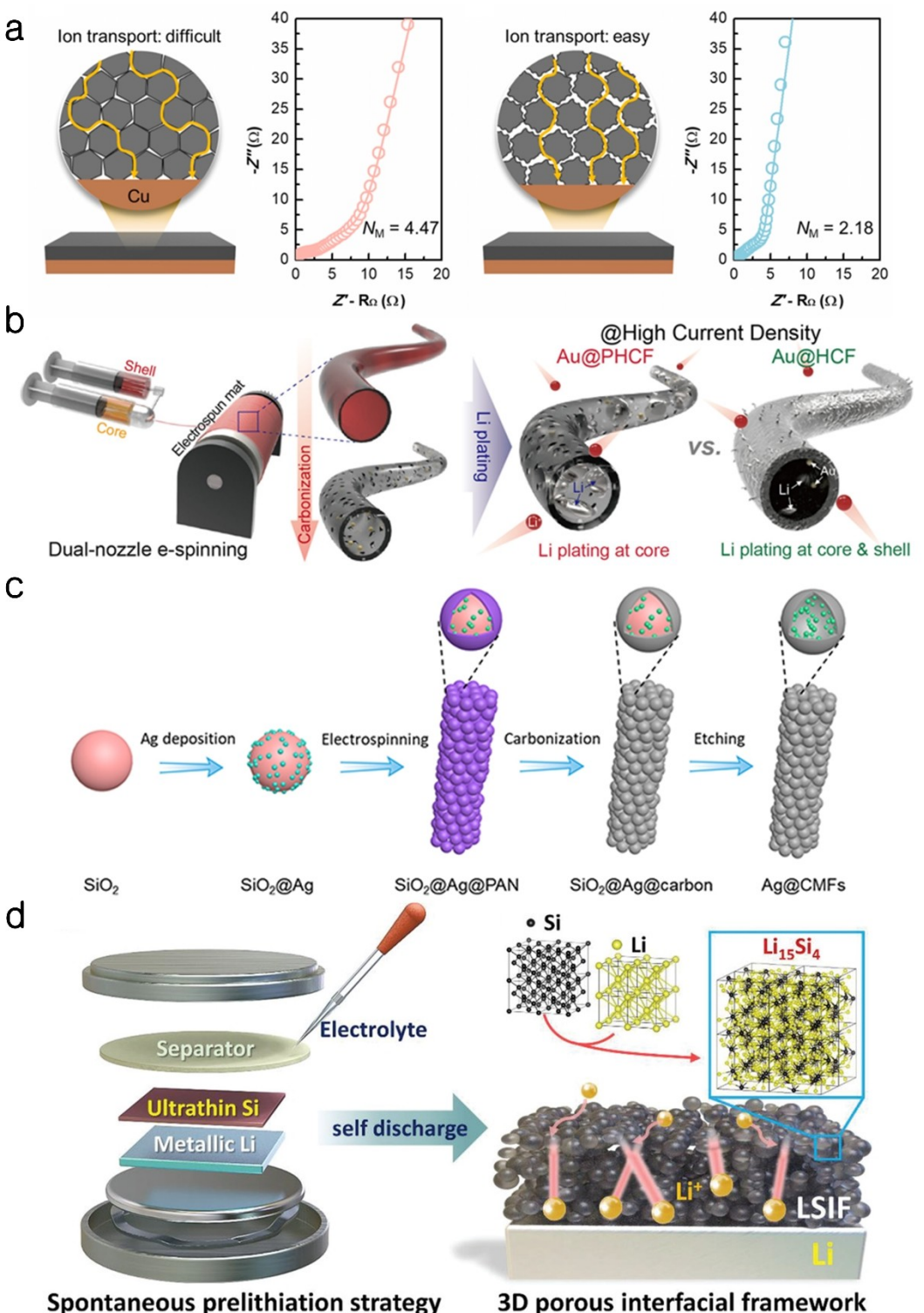


Figure 4. a) Faster lithium-ion transport kinetics inside the surface-functionalized porous 3D framework. Reproduced from ref. [53] Copyright (2021), with permission from Elsevier Inc. b) Confined lithium deposition inside the Au coated porous hollow carbon fibers. Reproduced from ref. [56] Copyright (2022), with permission from American Chemical Society. c) Fabrication process of Ag nanoparticle-embedded, nitrogen-doped carbon as 3D framework. Reproduced from ref. [57] Copyright (2021), with permission from American Association for the Advancement of Science. d) Enhanced lithium-ion diffusion inside the Li–Si alloy framework. Reproduced from ref. [58] Copyright (2021), with permission from Wiley-VCH.

2.4. Advanced electrolytes enhancing charge transport kinetics

The solvation structure of the electrolyte plays a crucial role in determining charge transfer kinetics of lithium-ions during electrodeposition.^[59] Advanced solvents and electrolyte additives can alter ion mobility and affect the surface chemistry, thereby influencing the overall lithium morphology and battery performance.^[60] For this reason, weakly solvating electrolytes, which typically consist of a high concentration of lithium salt (> 1.5 M) dissolved in ether or carbonate-based solvents, have been widely examined.^[61,62] Their unique anion-rich solvation structure facilitates lithium-ion desolvation, leading to the formation of a F-rich, thin, and rigid SEI layer that effectively suppresses lithium dendrite growth. Moreover, the redox potential of Li/Li⁺ can also be controlled by modulating the

solvation structures of lithium-ions, because the activity of lithium-ions varies with surrounding mediums, such as ion-solvent interaction and ion-ion interaction. Consequently, according to the Nernst equation, electrolytes with weakly solvating lithium-ion have a higher Li/Li⁺ redox potential than electrolytes with strongly solvating lithium-ions.^[63–65] This implies that the reductive decomposition of weakly solvating electrolytes on the lithium metal surface is significantly suppressed compared to strongly solvating electrolytes, resulting in the formation of stable SEI layer. In this regard, the Cui group has suggested that the utilization of a weakly solvated electrolyte increased the surface energy of lithium, thereby thermodynamically favoring uniform plating of lithium metal (Figure 5a).^[66] Therefore, designing advanced electrolytes and understanding the role of the solvation structure of the

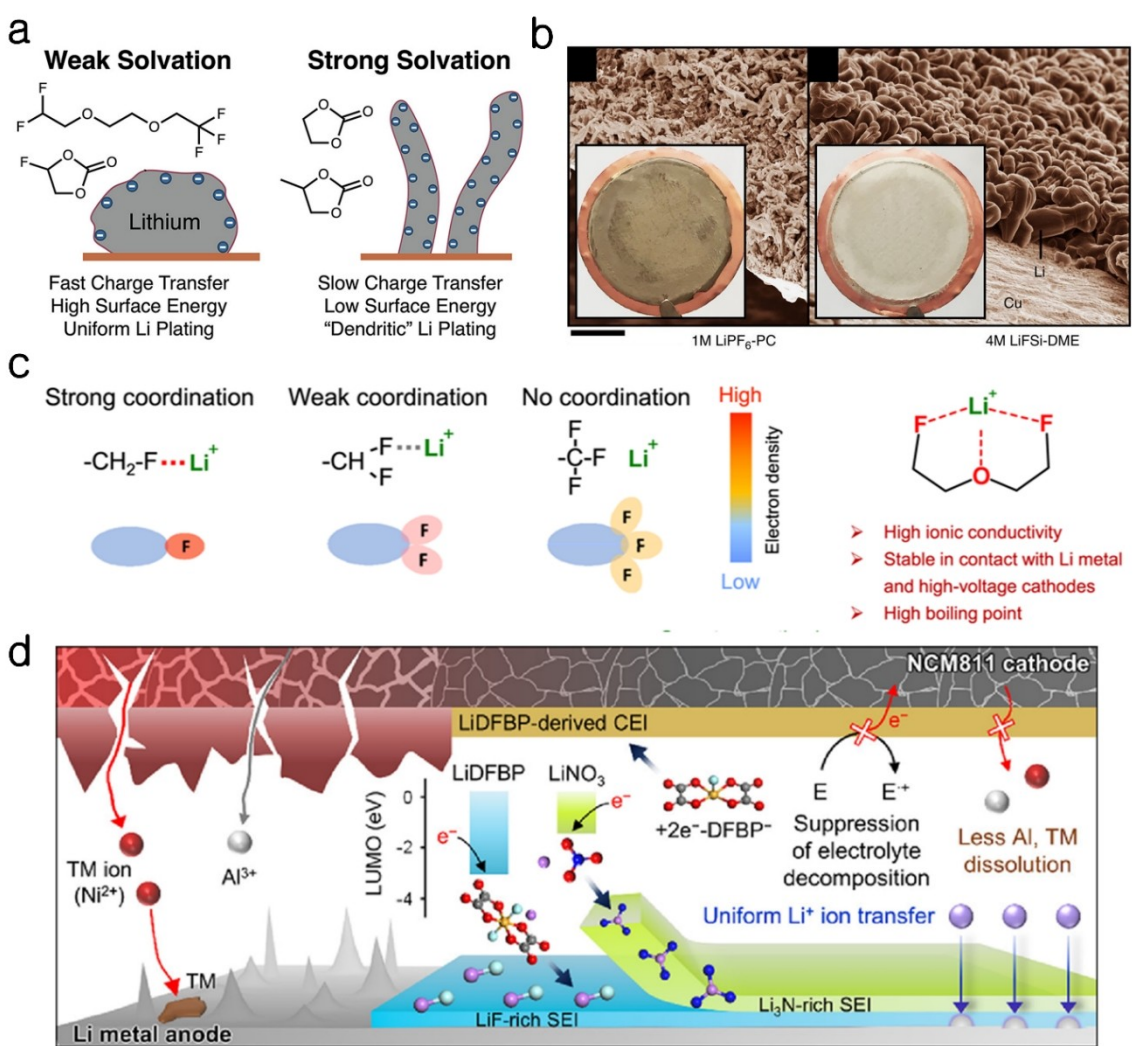


Figure 5. a) Correlation between lithium-ion solvation structure and lithium deposition morphology. Reproduced from ref. [66] Copyright (2022), with permission from American Chemical Society. b) Compact lithium deposition morphology in highly concentrated electrolyte compared to dendritic morphology in conventional electrolyte. Reproduced from ref. [68] Copyright (2015), with permission from Springer Nature. c) Formation of weakly solvating structure in monofluoro bis(2-fluoroethyl) ethers (BFE) solvent. Reproduced from ref. [78] Copyright (2023), with permission from Springer Nature. d) Dual-SEI layer composed of LiDFBP-derived inner-SEI layer and LiNO₃-derived outer-SEI layer, improving lithium metal performance. Reproduced from ref. [80] Copyright (2022), with permission from Elsevier Inc.

electrolyte are essential to mitigate lithium dendrite growth and to establish a robust SEI in LMBs.

The high concentration electrolyte (HCE) and localized high concentration electrolyte (LHCE) have been intensively investigated to reduce the amounts of uncoordinated solvents, because they are prone to reductive decomposition on the lithium metal surface, leading to undesirable side reactions.^[67] In this regard, Qian et al. utilized a 4 M lithium bis(fluorosulfonyl)imide (LiFSI) in DME for high rate applications of the LMA.^[68] The high concentration of LiFSI in the electrolyte regulated the lithium-ion solvation structure, promoting the formation of anion-rich SEI components. This contributed to a high coulombic efficiency and compact deposition morphology (Figure 5b). Consequently, the Li | Li symmetric cell showed cycling even at an exceptionally high rate of 10 mA cm^{-2} for over 6000 cycles. Dong et al. used 2,2,2-trifluoroethyl-1,1,2,3,3,3-hexafluoropropyl ether (THE) as a cosolvent with 1 M LiTFSI in DOL/DME (1:1, v/v).^[69] The electron-withdrawing group of THE reduced the interaction between lithium-ions and ether electrolytes, resulting in a weakly solvating structure. In combination with LFP, the Li | LFP full cell demonstrated 0.0012% capacity loss after 5,000 cycles at a 10 C.

Extensive research has been conducted on strategies for designing new types of electrolyte solvents, forming weakly solvating structures, and achieving stable SEIs, including fluorinated 1,4-dimethoxylbutane (FDMB),^[70] 1,2-diethoxyethane (DEE),^[71] fluorinated 1,2-diethoxyethane (FDEE),^[72] 1,1,1-trifluoro-2,3-dimethoxypropane (TFDMP),^[73] 2,2-dimethoxy-4-(trifluoromethyl)-1,3-dioxolane (DTDL),^[74] N,N-dimethylsulfamoyl fluoride (FSA),^[75] N,N-dimethyltrifluoromethane-sulfonamide (DMTMSA),^[76] and 3,3,4,4-tetrafluorotetrahydrofuran (TFF).^[77] They showed remarkably excellent electrochemical performances for LMBs. In particular, Zhang et al. reported monofluoride bis(2-fluoroethyl) ethers (BFE) as electrolyte solvents, showing excellent electrochemical performance under fast charging condition because of its highest ionic conductivity among nonaqueous solvents (8 mS cm^{-1}) and high lithium-ion transference number ($t_{\text{Li}^+} = 0.57$).^[78] The ionic conductivity of electrolytes is significantly influenced by their solvation structure,^[79] and thus, the monofluoro substituent ($-\text{CHF}_2$) in BFE enhances lithium-ion conductivity by maximizing the coordination interaction of fluorine atoms with lithium-ions (Figure 5c). Consequently, by using this advanced electrolyte, Li | NCM811 full cell (3.5 mAh cm^{-2}) demonstrated stable cycling over 200 cycles at a current density of 7 mA cm^{-2} . Electrolyte additives can also play an important role in improving the stability of the SEI, leading to improved cyclability, suppressed dendritic growth of lithium metal, and enhanced safety during fast charging. The Choi group proposed the formation of dual-layer SEI in ether electrolytes containing lithium difluoro(bisoxalato) phosphate (LiDFBP) and lithium nitrate (LiNO₃) (Figure 5d).^[80] Due to the high electron affinity of LiDFBP (-3.19 eV), LiDFBP was initially reductively decomposed, forming an inner SEI layer, which effectively improves mechanical durability and suppresses lithium dendrites. Then, LiNO₃ was reduced by accepting electrons from two-electron reduced DFBP⁻ species ($+2\text{e}^- \text{DFBP}^-$), resulting in the formation of a

LiNO₃-derived outer SEI layer. Furthermore, $+2\text{e}^- \text{DFBP}^-$ undergoes oxidative decomposition on the cathode surface, forming a stable cathode-electrolyte interphase (CEI) layer. The DFBP-derived CEI layer enhanced the oxidative stability against the ether solvent. This electrolyte showed the excellent rate performance of the Li | NCM811 full cell (2.6 mAh cm^{-2}), such as a high discharge capacity of approximately 160 mAh g^{-1} at a 5 C rate, which was higher than that of additive-free electrolyte (approximately 130 mAh g^{-1}).

Electrolyte modification emerges as the optimal approach to satisfy both fast charging capability and high energy density demand. Nonetheless, commercially employing these advanced electrolytes presents several issues, including poor wettability, high cost, and continuous consumption of lithium salts and additives during cycling.^[81,82] Therefore, the development of a new type of electrolyte should be accompanied by a combination with other advanced strategies, which were introduced in former sections, for the practical application of LMB under fast charging conditions.

3. Fast Charging in All-Solid-State Lithium Metal Batteries

Several key requirements must be considered when assessing the viability of solid-state electrolytes for use in energy storage applications. These requirements include ionic conductivity, chemical and electrochemical stability, thermal stability, mechanical strength, flexibility, low interfacial resistance, scalability, production costs, and safety. To address these complex considerations, researchers have extensively investigated various types of SEs, including oxides, sulfides, halides, and polymer electrolytes. Comprehensive summaries of each type of SE are also provided in Table 1.

SEs, which function as single-ion conductors, have a t_{Li^+} value of approximately 1.0, and the ionic conductivities of SEs, such as LGPS ($> 5.1 \text{ mS cm}^{-1}$) and LPSCl ($> 6.2 \text{ mS cm}^{-1}$) are comparable to those of commercial liquid electrolytes at room temperature.^[83,84] For this reason, ion depletion on the lithium metal surface cannot theoretically occur in SEs even at high current densities. Furthermore, the exchange current density of lithium metal/solid-state electrolyte, such as Li/LLZO and Li/Li₂S-P₂S₅, exceeds 50 mA cm^{-2} ,^[85,86] indicating fast charge transfer kinetics of lithium-ions between solid/solid interface. Despite these theoretical backgrounds, dendritic growth of lithium metal were frequently observed in ASSLMBs, leading to the internal short circuits even at a moderate current density ($< 1 \text{ mA cm}^{-2}$).^[87]

Critical current density (CCD) is a widely used parameter to assess the rate capability of ASSLMBs, representing the maximum endurable current density during cycling without a short circuit.^[88] Recent studies have reported that CCD is predominantly influenced by the characteristics of the SE/LMA interface.^[89,90] In this regard, the formation of pores and defects between SE and lithium metal is a significant factor affecting dendritic growth of lithium metal. Recently, Ning et al.

Table 1. Comparison of various types of solid-state electrolytes.

Type	Materials	Ionic conductivity [S cm^{-1}]	Thermal stability [°C]	Chemical stability	Electrochemical stability [V vs. Li/Li ⁺]	Mechanical strength [GPa]	Production cost [\$/g]
Oxide	perovskite $\text{Li}_{3.3}\text{La}_{0.56}\text{TiO}_3$ LISICON $\text{Li}_{14}\text{Zn}(\text{GeO}_4)_4$ NASICON $\text{LiTi}_2(\text{PO}_4)_3$ garnet $\text{Li}_7\text{La}_3\text{Zr}_2\text{O}_{12}$	$10^{-7}\text{--}10^{-3}$	800–1500	stable	0–4 V	100–200	5–10
Sulfide	argyrodite $\text{Li}_6\text{PS}_5\text{Cl}$ LISICON-like $\text{Li}_{10}\text{GeP}_2\text{S}_{12}$ $\text{Li}_2\text{S}\text{-P}_2\text{S}_5$ system 0.7Li ₂ S–0.3P ₂ S ₅	$10^{-6}\text{--}10^{-2}$	500–700	sensitive to air and moisture poor compatibility towards high-polarity solvent and binder	1–3 V	20–40	5–30
Halide	chloride Li_3YCl_6 iodide LiI anti-perovskite Li_3OCl spinel Li_2ZnI_4	$10^{-6}\text{--}10^{-3}$	> 400	sensitive to moisture	0.5–7 V	20–50	5–160
Polymer	PEO-based PEO/LiTFSI copolymer (PEO-PEI)/LiClO ₄ crosslinked (PEO-PSI)/LiCF ₃ SO ₃	$10^{-7}\text{--}10^{-4}$	200–500	stable	0.5–6.5 V	$10^{-4}\text{--}10^{-3}$	0.5–2
References	–	[97]	[98]	[99]	[100–101]	[102–103]	[104]

proposed a dendrite-induced cell failure mechanism involving two separate processes: crack initiation induced by sub-surface pore filling and crack propagation induced by wedge opening, which differs from the previous model: lithium-tip driven crack formation.^[91] Specifically, the initiation of dendrites is influenced by the microscopic fracture strength present at the boundaries of the SE, and this influence is dependent on factors such as pore size, pore density, and current density. On the contrary, the propagation of dendrites is contingent on the macroscopic fracture strength of the SE, which is impacted by factors like the length of the dendrite, current density, and stack pressure. Additionally, poor contact between SE/LMA interface, loss of intimate physical contact after repeated cycles, parasitic chemical and electrochemical reaction have also been considered as potential issues hindering the practical application of ASSLMBs.^[92–94] The following sections will introduce recent advances to address the aforementioned issues in detail.

3.1. Interlayer between electrode and electrolyte

Recent studies have demonstrated that micro-cracks, pores, and grain boundaries of the SE are preferential sites for lithium dendrite growth.^[95,96] Moreover, poor adhesion and void formation between the SE and LMA during repetitive cycling gave rise to a significant increase in the local current density of the contacted area, leading to cell failure.^[105,106] For example, Bucci et al. proposed a theoretical model that demonstrated the influence of the surface geometry of SE on the kinetic properties of the SE/LMA interface.^[107] They determined the current density associated with lithium electrodeposition on the electrolyte layer, considering the geometry and resistance of the interface as variables using finite element analysis equations.

$$\Delta\varphi = 0 \text{ on } \Omega \quad (2)$$

$$\nabla\varphi \cdot \mathbf{n} = h(\varphi - \varphi_{Li}) \text{ on } \partial\Omega_- \quad (3)$$

$$\nabla\varphi \cdot \mathbf{n} = \bar{i} \text{ on } \partial\Omega_+ \quad (4)$$

Equations (2), (3), and (4) imply steady-state conduction across the electrolyte, linearized Butler-Volmer kinetics, and uniform current at the positive electrode interphase, respectively. In the equation, Ω , $\partial\Omega_-$, $\partial\Omega_+$, φ , φ_{Li} , h , and \bar{i} are the bulk electrolyte phase, negative electrode interface, positive electrode interface, potential of the lithium, potential of the lithium in lithium metal interphase, convective coefficient, and the ratio between the current density and the electrolyte bulk conductivity, respectively. According to the equation, the current is concentrated at the crack tip, with wider cracks resulting in greater localized current (Figure 6a). For this reason, it is vital to enhance the contact properties, and thus considerable efforts have been devoted to creating a stable interlayer between the SE/LMA interface.

Among them, LiF has been widely examined as an interlayer between the solid electrolyte and the lithium metal because it can effectively suppress electron leakage due to its large band gap and improve the transport kinetics of lithium-ions.^[108] The Kang group used vacuum thermal evaporation to apply Ag and LiF layers on the garnet-type $\text{Li}_{6.4}\text{La}_3\text{Zr}_{1.4}\text{Ta}_{0.6}\text{O}_{12}$ (LLZTO) pellets (Figure 6b).^[109] The Ag layer served as a lithophilic host, improving lithium wettability and decreasing interfacial resistance. The LiF layer with low electronic conductivity, effectively blocked the electron pathway between lithium and the SE. Consequently, the Ag/LiF-coated multifunctional interlayer enabled a CCD of 3.1 mA cm^{-2} , which is about 2 times higher than the Ag-coated interlayer (1.5 mA cm^{-2}). Similarly, they also proposed a multifunctional interface composed of a Li–Sn alloy and LiF on the garnet-type $\text{Li}_{6.4}\text{La}_3\text{Zr}_{1.4}\text{Ta}_{0.6}\text{O}_{12}$ (LLZTO). The

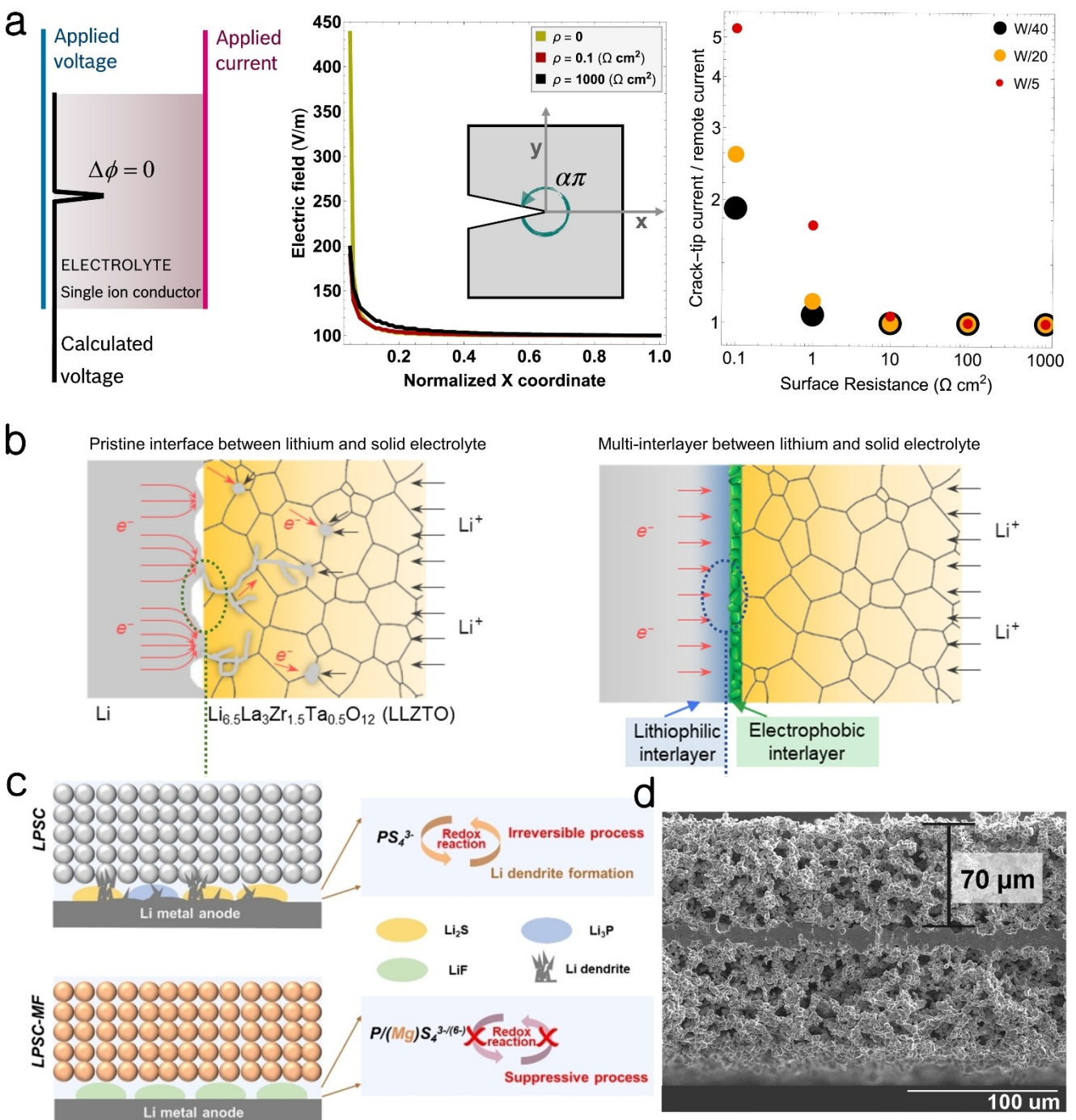


Figure 6. a) A schematic illustration of Equations (2)–(4) is provided, representing the electric field applied at the crack tip of the solid-state electrolyte and the relationship between crack size and the applied current density. Reproduced from ref. [107] Copyright (2019), with permission from Elsevier Inc. b) Dendrite growth behavior at the interface between solid-state electrolyte and lithium metal electrode with and without Ag/LiF interlayer. Reproduced from ref. [109] Copyright (2021), with permission from American Association for the Advancement of Science. c) Suggested mechanism for suppressing reductive decomposition of LPSC-MF electrolyte. Reproduced from ref. [120] Copyright (2023), with permission from Wiley-VCH. d) Cross sectional SEM image of porous dense-porous trilayer. Reproduced with ref. [122] Copyright (2019), with permission from Elsevier Inc.

surface of the SE was wet-coated with a SnF₂-dispersed solution, followed by heating at 220°C while in contact with lithium metal. This process led to a chemical conversion reaction, resulting in the formation of an interphase consisting of Li-Sn alloy and LiF. The conformal LiF layer functioned as an electron

insulator at the SE/LMA interface and also reduced interfacial resistance, thereby facilitating lithium-ion diffusion kinetics. The Li-Sn alloy further promoted lithium-ion transfer via chemical diffusion. Owing to this synergistic effect, the Li|SnF₂-treated LLZTO|Li symmetric cell exhibited a CCD of 2.4 mA cm⁻² at

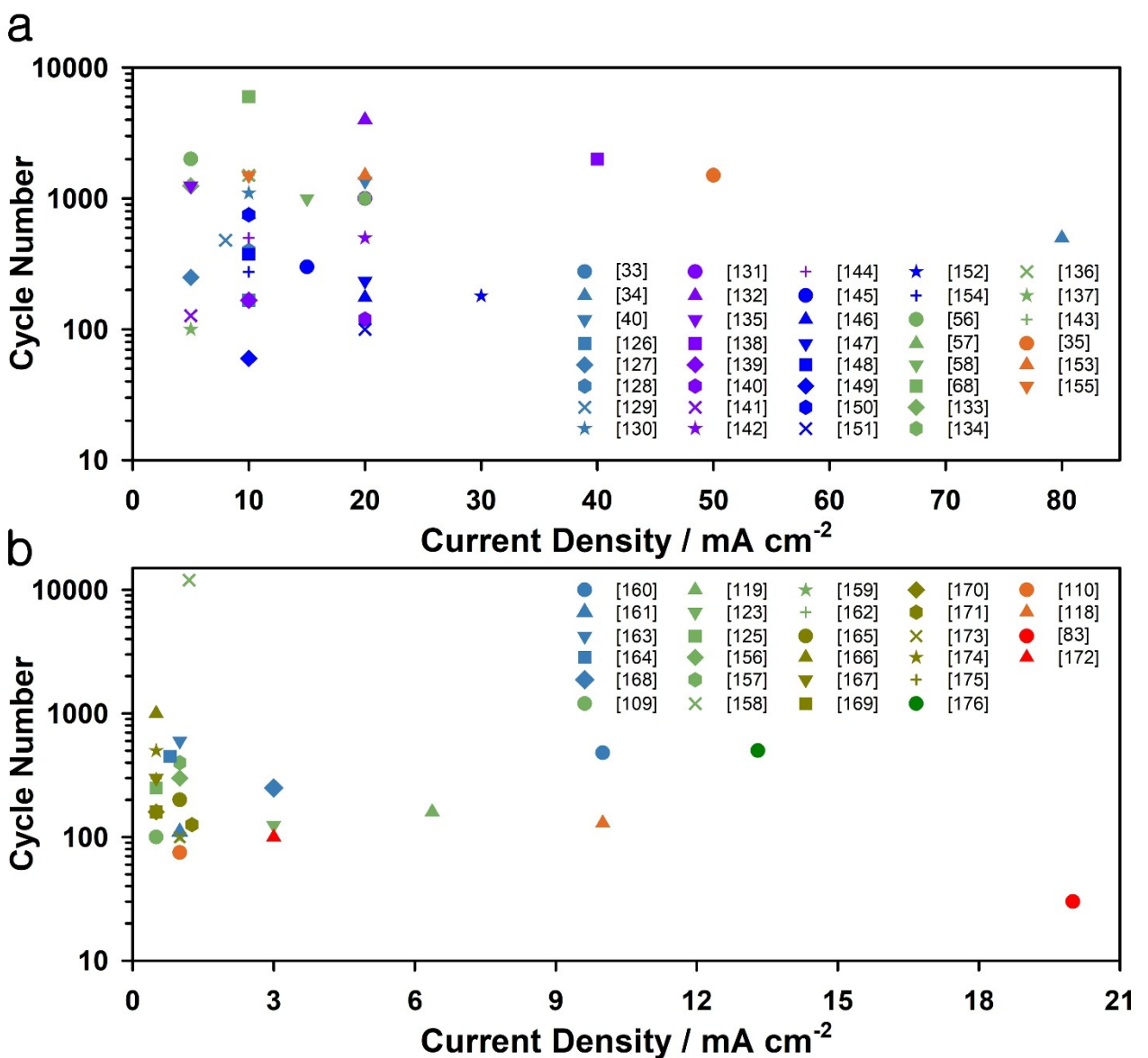


Figure 7. Summary of cycle performance of lithium metal electrodes with a) liquid electrolytes at a current density over 5 mA cm^{-2} and b) solid-state electrolytes at a current density over 0.5 mA cm^{-2} , as reported in previous literature. The number in the brackets refers to the reference number. Each color represents operating temperature (Green: 25°C , Orange: 30°C , Red: over 50°C , Blue and purple: undefined)

room temperature. In addition, Su et al. introduced lithium phosphorous oxynitride (LiPON) interlayer to alleviate contact issues at the interface between LPSCl and lithium metal.^[110] The LiPON-coated LPSCl was fabricated without grain boundaries and pores using radio frequency sputtering. The resulting LiPON thin-film exhibited good lithium-ion conductivity ($\approx 1 \mu\text{S cm}^{-1}$) and electron insulation ($\approx 10^{14} \Omega\text{cm}$), with low interfacial resistance ($1.3 \Omega\text{cm}^2$) due to its high wettability with the lithium metal electrode. As a result, the CCD of the $\text{Li} \mid \text{LiPON/LPSCl} \mid \text{Li}$ symmetric cell reached 4.1 mA cm^{-2} at 30°C , demonstrating excellent rate performance.

It is also remarkable that the Ag–C layer has demonstrated its effectiveness in advancing the technology of all-solid-state batteries (ASSBs), which is attributed to its ability to suppress dendrite formation of lithium metal.^[111,112] Recently, Samsung

Co. demonstrated the excellent cell performance of ASSBs using an Ag–C composite interlayer for anode-free ASSBs.^[113] This achievement represents a significant advancement towards the commercialization of ASSBs. Compared to the bare SUS current collector, on which lithium was deposited in thick and randomly distributed shape, lithium was densely deposited on the bottom of the Ag–C nanocomposite layer even at a high current density of 3.4 mA cm^{-2} . TEM and EELS analyses supported that Ag facilitated the transport of lithium as a lithophilic host. Moreover, carbon served as a spacer preventing direct contact between the LPSCl and the LMA. Warm isostatic pressing (WIP) was also applied during cell fabrication to alleviate the contact issue between the electrode and electrolyte layers. As a result, the pouch-type Ag–C | NCM full cell demonstrated extraordinary cell performance, operating for over 1,000 cycles at a

Table 2. Summary of electrochemical performances of lithium metal electrodes with liquid electrolytes at a current density over 5 mA cm⁻².

Reference	Strategy	Electrolyte	Current density [mA cm ⁻²]	Capacity [mAh cm ⁻²]	Cycle retention (number)	Temperature [°C]
[33]	Electronegative nanochannels separator	1 M LiPF ₆ in EC/DMC/EMC (1:1:1, v/v/v)	5	2.5	2000	–
[34]	Thermally conductive AlN nanowires onto the commercial polypropylene separator	1 M LiTFSI in DOL/DME (1:1, v/v)+2 wt% LiNO ₃	80	80	500	–
[35]	Hierarchically porous aramid nanofiber separators	1 M LiPF ₆ in EC/DEC/DMC (1:1:1)	50	1	1500	30
[40]	Hybrid SEI (Li ₃ Sb + LiF)	1 M LiTFSI in DOL/DME (1:1, v/v)+2 wt% LiNO ₃	20	2	1360	–
[56]	1D porous Li-confinable host with lithophilic Au	LiFSI-1.2DME-3TTE (in molar ratio)	5	1	2000	25
[57]	Ag nanoparticle-embedded nitrogen-doped carbon macroporous fibers	1 M LiTFSI in DOL/DME (1:1, v/v)+2 wt% LiNO ₃	10	2	750	25
[58]	3D porous Li-Si interfacial framework	1 M LiTFSI in DOL/DME (1:1, v/v)	15	1	1000	25
[68]	Highly concentrated electrolyte	4 M LiFSI in DME	10	0.5	6000	25
[126]	Graphite fluoride-LiF protective layer	1 M LiPF ₆ in EC/DEC (1:1)	10	1	167	–
[127]	c-PEGDMA protective film	1 M LiPF ₆ in EC/DEC (1:1)	5	5	250	–
[128]	Sn coating	1 M LiTFSI in DOL/DME (1:1, v/v)+1 wt% LiNO ₃	10	1	400	–
[129]	Lithiated Nafion/LiCl interface	1 M LiTFSI in DOL/DME (1:1, v/v)+1 wt% LiNO ₃	8	1	480	–
[130]	2D Ti ₃ C ₂ T _x MXene stacks coating	1 M LiTFSI in DOL/DME (1:1, v/v)+0.1 M LiNO ₃	10	10	1100	–
[131]	Al-Li alloy protective layer	1 M LiTFSI in DOL/DME (1:1, v/v)+1 wt% LiNO ₃	20	1	1000	–
[132]	LiPEO-UPy layer	1 M LiTFSI in DOL/DME (1:1, v/v)+2 wt% LiNO ₃	20	1	4000	–
[133]	Ag/Li composite anode	1 M LiTFSI in DOL/DME (1:1, v/v)	5	1	1250	25
[134]	Li-Sn alloy/PVDF-HFP protective film	1 M LiTFSI in DOL/DME (1:1, v/v)	20	1	1000	25
[135]	LiAl alloy-based interfacial layer	1 M LiPF ₆ in EC/DEC (1:1, v/v)	5	1	1250	–
[136]	PTCDI organic layer	1 M LiTFSI in DOL/DME (1:1, v/v)	10	1	1500	25
[137]	Dual-layered film	1 M LiPF ₆ in EC/DEC (1:1, v/v)	5	0.5	100	25
[138]	CuO nanoflowers on Ti-mesh	1 M LiTFSI in DOL/DME (1:1, v/v)	40	1	2000	–
[139]	Multichannel carbon fiber paper with Au modification	1 M LiTFSI in DOL/DME (1:1, v/v)+2 wt% LiNO ₃	10	30	167	–
[140]	Hierarchical 3D Co ₃ O ₄ -CS framework	1 M LiTFSI in DOL/DME (1:1, v/v)	20	1	120	–
[141]	3D nanoporous N-doped graphene	1 M LiTFSI in DOL/DME (1:1, v/v)+1 wt% LiNO ₃	5	10	127	–
[142]	Hydrophobic graphene framework	1 M LiPF ₆ in EC/DMC	20	1	500	–
[143]	Lithium-expanded graphite composite	1 M LiTFSI in DOL/DME (1:1, v/v)+1 wt% LiNO ₃	10	1	1500	25
[144]	Carbonized eggplant host	1 M LiPF ₆ in EC/DEC (1:1, v/v)+10 wt% FEC+1 wt% VC	10	1	500	–
[145]	Carbon nanotubes in melamine sponges	1 M LiTFSI in DOL/DME (1:1, w/w)+2 wt% LiNO ₃	15	15	300	–
[146]	3D Ti ₃ C ₂ T _x MXene-melamine foam	1 M LiTFSI in DOL/DME (1:1, v/v)+1 wt% LiNO ₃	20	20	175	–

Table 2. continued

Reference	Strategy	Electrolyte	Current density [mA cm^{-2}]	Capacity [mAh cm^{-2}]	Cycle retention (number)	Temperature [$^{\circ}\text{C}$]
[147]	MXene/graphene framework	1 M LiTFSI in DOL/DME (1:1, v/v) + 1 wt% LiNO ₃	20	5	234	-
[148]	3D printed N-doped carbon framework	1 M LiTFSI in DOL/DME (1:1) + 1 wt% LiNO ₃	10	2	375	-
[149]	Self-supporting Li-Sn-Sb foil	1 M LiPF ₆ in EC/DEC (1:1, v/v) + 10% FEC + 1% VC	10	10	60	-
[150]	3D printed vertically aligned Li anode	1 M LiTFSI in DOL/DME (1:1, v/v) + 1 wt% LiNO ₃	10	10	750	-
[151]	Mesoporous AlF ₃ framework	1 M LiPF ₆ in EC/DEC + 10% FEC + 1% VC	20	1	100	-
[152]	In situ formation of SrF ₂ layer	2 M LiFSI in DME	30	1	180	-
[153]	Flexible active solid electrolyte interphase layer	1 M LiPF ₆ in EC/DMC/EMC (1:1:1, v/v/v)	20	2	1500	30
[154]	Li metal anode treated with zirconyl nitrate ($\text{LiZrO}(\text{NO}_3)_2 @ \text{Li}$)	1 M LiTFSI in DOL/DME (1:1, v/v) + 2 wt% LiNO ₃	10	10	275	-
[155]	Boron-doped electrolytes	1 M LiPF ₆ in EC/DMC (1:1, v/v)	10	1	1500	30

current density of 3.4 mA cm^{-2} and an areal capacity of 6.8 mAh cm^{-2} .

3.2. Chemical/electrochemical stabilities at the interface

Solid-state electrolytes, such as LPSCI and LGPS, are known to exhibit an unstable interface upon contact with highly reductive lithium metal because of their narrow electrochemical stability window.^[114] This instability leads to the formation of electrolyte decomposition byproducts, including Li₃P, Li₂S, LiCl, and Li₁₅Ge₄.^[115] In particular, at the interface between LGPS and lithium metal, electrolyte decomposition was accelerated by the formation of a mixed-conducting interphase (MCI), such as Li–Ge alloys, that conducts both electrons and ions.^[116] In this regard, Su et al. introduced a simple graphite interlayer consisting of 95% graphite and 5% PTFE to avoid direct contact between Li₁₀GeP₂S₁₂ (LGPS) and lithium metal.^[117] This layer also offered endurance against pressure-induced stress, enabling the application of high stacking pressure of 250 MPa. Thus, the cell exhibited no signs of short-circuits, even after applying a high current density of 10 mA cm^{-2} while examining rate performance. Ye et al. proposed a sandwich-type multilayer design of solid-state electrolyte, LPSCI-LGPS-LPSCI, in which LPSCI inhibited the direct contact between LGPS and lithium metal.^[83] The middle LGPS layer also had a function of suppressing the propagation of lithium dendrites through the solid electrolyte membrane due to high reactivity of LGPS with lithium metal. Consequently, the Li | NCM811 full cell with the multilayer electrolyte retained 82% of its capacity after 10,000 cycles at a high rate of 20 C.

In addition, the modification of solid electrolytes through doping has been intensively investigated to improve the

chemical stability of LPSCI, mitigating side reactions between the LPSCI and the LMA. For example, Taklu et al. fabricated iodized-oxychloride sulfide electrolyte by employing oxygen doping with fumy iodine additive (Li₆PS_{4.8}O_{0.2}Cl–5 wt% I₂).^[118] In-situ formed SEI composed of Li₂O and LiI contributed to suppressing reductive decomposition of electrolyte against lithium metal. As a result, the Li | Li₆PS_{4.8}O_{0.2}Cl–5 wt% I₂ | Li symmetric cell showed stable cyclability over 260 hours at a current density of 10 mA cm^{-2} and an areal capacity of 10 mAh cm^{-2} . Zhao et al. introduced the fluorination of LPSCI by partially substituting LiCl with LiF (Li₆PS₅Cl_{0.3}F_{0.7}).^[119] The Li₆PS₅Cl_{0.3}F_{0.7} electrolyte showed condensed morphology without voids due to the lower bonding energy of P–S and Young's modulus. Moreover, the F substitution gave rise to the formation of the robust LiF-based SEI layer, effectively suppressing dendritic growth of lithium metal. The Li | Li₆PS₅Cl_{0.3}F_{0.7} | Li symmetric cell exhibited stable capacity retention over 250 hours at a high current density of 6.37 mA cm^{-2} and an areal capacity of 5 mAh cm^{-2} . Liu et al. demonstrated the redox resistible LPSCI by incorporating MgF₂ (LPSC-MF) to inhibit the irreversible decomposition of PS₄³⁻.^[120] The presence of a Mg atom within the tetrahedral arrangement of the crystal structure leads to s-p hybridization. This hybridization prevents the acceptance of electrons from lithium atoms, thus impeding the irreversible redox reaction of LPSCI, which, in turn, hinders its decomposition into Li₂S and Li₃P (Figure 6c). As a result, the Li | LPSC-MF | Li symmetric cell exhibited a CCD of 1.4 mA cm^{-2} , which is approximately 2.3 times higher than that of the pristine LPSCI electrolyte at 25 °C. Moreover, the surface modification of solid electrolytes also enhance their chemical and electrochemical stability against LMA. Kim et al. introduced a straightforward surface modification of LPSCI using a solution-based adsorption with 2-trimethylsilylthiol (TMS-SH) through chalco-

Table 3. Summary of electrochemical performances of lithium metal electrodes with solid-state electrolytes at a current density over 0.5 mA cm⁻².

Reference	Strategy	Electrolyte	Current density [mA cm ⁻²]	Capacity [mAh cm ⁻²]	Cycle retention (number)	Temperature [°C]
[83]	Sandwiched structure	Li _{5.5} PS _{4.5} Cl _{1.5} /Li ₁₀ GeP ₂ S ₁₂	20	0.25	30	55
[109]	Ag/LiF-coating	Li _{6.4} La ₂ Zr _{1.4} Ta _{0.6} O ₁₂	0.5	0.25	100	25
[110]	LiPON interlayer	Li ₆ PS ₅ Cl	1	1	75	30
[118]	Iodized-oxychloride argyrodite	Li ₆ PS _{4.8} O _{0.2} Cl-5 wt% I ₂	10	10	130	30
[119]	Fluorination of Li ₆ PS ₅ Cl	Li ₆ PS ₅ Cl	6.37	5	160	25
[123]	Amorphous-Carbon-Coated 3D Solid Electrolyte	Li _{6.75} La ₃ Zr _{1.75} Ta _{0.25} O ₁₂	3	6	125	25
[125]	3D-micropatterned SSE	Ta-doped Li ₇ La ₃ Zr ₂ O ₁₂	0.5	0.5	250	25
[156]	Wet-coated SnF ₂ particles	Li _{6.4} La ₂ Zr _{1.4} Ta _{0.6} O ₁₂	1	0.5	300	25
[157]	Elastic and Li ⁺ -conducting interlayer	Li _{6.5} La ₃ Zr _{1.5} Ta _{0.5} O ₁₂	1	0.5	400	25
[158]	Lithiophilic AgSn _{0.6} Bi _{0.4} O _x coating	Li _{6.5} La ₃ Zr _{1.5} Ta _{0.5} O ₁₂	1.2	0.1	12000	25
[159]	Li ₃ PO ₄ -Li ₃ N hybrid interphase	Li _{5.41} PS _{4.41} Cl _{1.59}	1	1	100	25
[160]	Ag nanoparticles	Li ₆ PS ₅ Cl	10	6.25	480	-
[161]	Li/garnet interface modified by AAO membranes	Li _{6.25} Ga _{0.25} La ₃ Zr ₂ O ₁₂	1	0.5	110	-
[162]	Ultra-thin Al-Si interface buffer layer	Li _{6.75} La ₃ Zr _{1.75} Ta _{0.25} O ₁₂	1	1	400	26
[163]	Bifunctional Co ₃ O ₄ layer on garnet-type	Li _{6.5} La ₃ Zr _{1.5} Ta _{0.5} O ₁₂	1	0.5	600	-
[164]	Bifunctional Cu-doped Li ₃ Zn composite layer	Li _{6.5} La ₃ Zr _{1.5} Ta _{0.5} O ₁₂	0.8	0.4	450	-
[165]	Flexible electron-blocking interfacial shield	Li _{6.4} La ₃ Zr _{1.4} Ta _{0.6} O ₁₂	1	1	200	25
[166]	Strontium (Sr) doping into lithium anodes	Li _{6.5} La ₃ Zr _{1.5} Ta _{0.5} O ₁₂	0.5	0.25	1000	25
[167]	3D Li-Zn alloy layer	Li _{6.4} La ₃ Zr _{1.4} Ta _{0.6} O ₁₂	0.5	0.25	300	25
[168]	In situ construction of 3D Li anode	Li ₆ PS ₅ Cl + LiAlCl ₄	3	3	250	-
[169]	Bilayer dense-porous LLZO membranes	Al-doped Li ₇ La ₃ Zr ₂ O ₁₂	0.5	0.25	160	25
[170]	Mixed solid electrolyte	Li _{5.5} PS _{4.5} Cl _{1.5} /Li ₁₀ SnP ₂ S ₁₂ (6:4, w/w)	0.5	0.25	160	25
[171]	Sn (IV) substitution for P (V) in Li ₆ PS ₅ I	Li _{6.2} P _{0.8} Sn _{0.2} S ₃ I	1.26	1	126	25
[172]	CuCl doped Li ₆ PS ₅ Cl	Li _{6.3} P _{0.9} Cu _{0.1} S _{4.9} Cl _{1.1}	3	3	100	50
[173]	N-doped Li ₆ PS ₅ Cl	Li _{6.25} PS _{4.75} N _{0.25} Cl	1	1	100	25
[174]	LiNO ₃ -doped Li ₃ PS ₄	Li _{2.96} P _{0.98} S _{3.92} O _{0.06} -Li ₃ N	0.5	0.5	500	25
[175]	Li ₂ WO ₄ additive	Li _{6.5} La ₃ Zr _{1.5} Ta _{0.5} O ₁₂	0.5	0.25	300	25
[176]	Removing impurity of the Li metal	Li _{6.4} La ₃ Zr _{1.4} Ta _{0.6} O ₁₂	13.3	0.4	500	25

gen-chalcogen interactions and hydrogen bonding between LPSCl and TMS-SH.^[121] The TMS-SH layer adsorbed onto the surface of LPSCl underwent electrochemical decomposition at approximately 4.2 V (vs. Li/Li⁺), leading to the formation of a stable passivation layer composed of silicon oxide (SiO_x) compounds. This stable layer effectively suppressed the chemical and electrochemical degradation of LPSCl, thereby mitigating the formation of sulfate and phosphate. Eventually, the Li | LPSCl-TMS-SH | LCO full cell exhibited stable cycle performance, with a capacity retention of 85 % after 2000 cycles.

3.3. Modification of solid-state electrolyte structures

Increasing the contact area between the electrode and electrolytes has a straightforward effect on reducing the local current density, which is particularly essential under fast charging conditions. Garnet-type electrolytes, which offers high electrochemical stability against lithium metal and superior mechanical properties, can serve as a fundamental building block for a three-dimensional solid-state electrolyte framework. The Wachsmann and Hu groups introduced a porous-dense-porous trilayer scaffold using garnet-type Li_{6.75}La_{2.75}Ca_{0.25}Zr_{1.5}Nb_{0.5}O₁₂ (Fig-

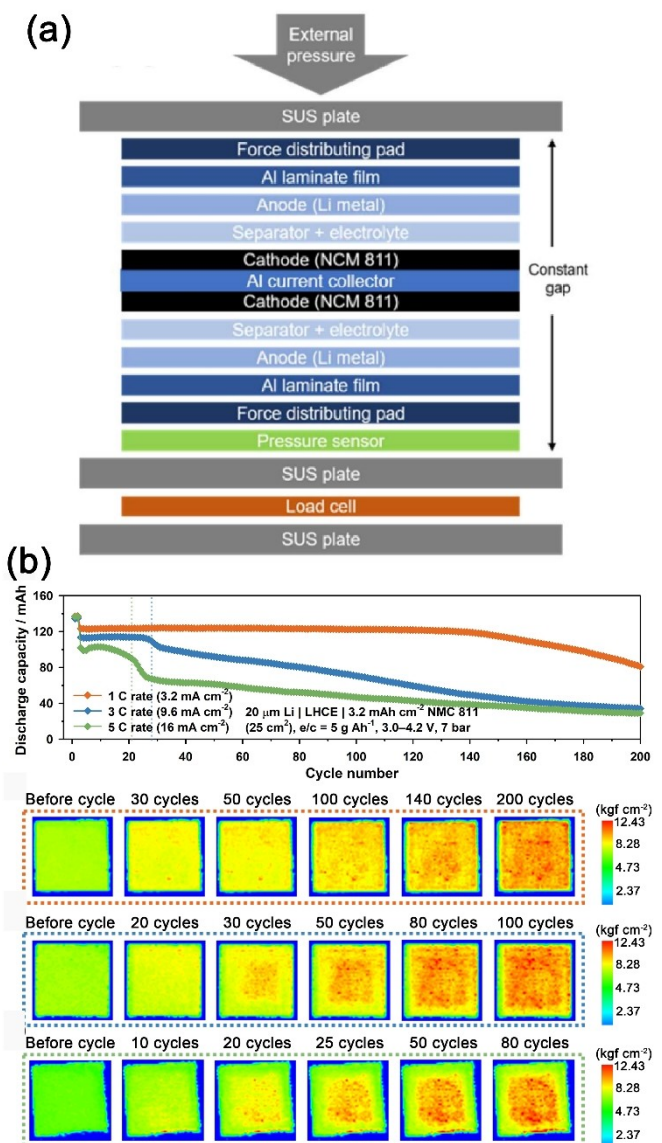


Figure 8. a) Schematic image of operando spatial pressure mapping analysis kit. b) Cycle performance and corresponding operando pressure mapping images of the pressurized Li | NMC811 pouch cells at various C rates. Reproduced with ref. [11] Copyright (2023), with permission from Wiley-VCH.

ure 6d).^[122] Each layer was fabricated using a simple tape-casting method, with two porous layers containing poly (methyl methacrylate) spheres as a porogen to achieve high porosity. The layers were then combined, heat-pressed at 60 °C, and sintered at a high temperature of 1050 °C. The resulting framework was further enhanced by coating it with Al₂O₃ using atomic layer deposition (ALD) to improve lithium wettability. Finally, molten lithium was introduced into pores for use as an anode. The thinly fabricated dense layer (14 µm) provided shorter lithium-ion conduction pathways and demonstrated a lower area-specific resistance (~2–10 Ω cm²), compared to a commercial 18650 full cell (22 Ω cm²). Moreover, this layer exhibited a pinhole-free morphology (>99% density), effectively preventing dendrite formation. The porous layer also

offered approximately 40 times the surface area of a planar cell, which played a crucial role in mitigating local current density. As a result, the symmetric Li | Li trilayer exhibited high rate cycling at 10 mA cm⁻² without a short circuit. Furthermore, they incorporated an amorphous carbon nanocoating on the porous-dense-porous trilayer structure consisting of garnet-type Li_{6.75}La₃Zr_{1.75}Ta_{0.25}O₁₂.^[123] The carbon coating established an electronic pathway throughout the porous layer, effectively homogenizing electron transport, and thus reducing residual lithium crystallites within the pores. Consequently, the Li | electrolyte | Li asymmetric cell with carbon coating demonstrated stable cycling at 3 mA cm⁻² over 125 cycles compared to an asymmetric cell without carbon coating, which exhibited a short circuit in less than 30 cycles, even at a lower current density of 0.05 mA cm⁻². However, the application of the second electron-conducting coating phase to the porous layer may have led to spallation at the coated interface. To address this issue, they recently proposed a single-phase mixed ion- and electron-conducting (MIEC) material for the porous layer.^[124] The MIEC garnet (Li_{6.4}Ga_{0.2}Pr₃Zr_{1.8}Ce_{0.2}O₁₂) was synthesized using a simple solid-state reaction. This involved the substitution of the La and Zr elements in the conventional garnet-type Li_{6.75}La₃Zr_{1.75}Ta_{0.25}O₁₂ (Ta-LLZ) with multivalent cations such as Pr and Ce, in addition to the doping of Ga into lithium interstitial sites. While the lithium-ion conductivity of MIEC garnet decreased to 0.092 mS cm⁻¹ compared to Ta-LLZ (0.23 mS cm⁻¹), its electronic conductivity increased by three orders of magnitude, from 1.6 nS cm⁻¹ to 7.2 µS cm⁻¹. This enhanced electronic conductivity serves as a facile electronic pathway. Consequently, the Li | MIEC–Ta-LLZ–MIEC | Li symmetric cell showed an unprecedented CCD exceeding 100 mA cm⁻², as well as stable cyclability of over 80 hours at a high current density of 60 mA cm⁻² and an areal capacity of 30 mAh cm⁻² at 25 °C. Xu et al. also designed a 200 µm scale 3D-micropatterned garnet-type Li_{6.4}La₃Zr_{1.4}Ta_{0.6}O₁₂ (3D-SSE) using a high-precision laser cutter.^[125] The interfacial resistance of the Li | 3D-SSE | Li cell (16.9 Ω cm²), measured by electrochemical impedance spectroscopy, decreased compared to the bare Li | SSE | Li cell (50.4 Ω cm²), which was attributed to a higher effective contact area (~2.5 times). Moreover, finite element analysis showed increased stress at the trench region of 3D-SSE, which acted as an additional force for lithium metal creep, preventing the mechanical degradation of the LMA/SE interface. The Li | 3D-SSE | Li symmetric cell exhibited stable cycling over 250 cycles at a current density of 0.5 mA cm⁻².

4. Summary and Outlook

We summarized recent progress in lithium metal batteries with liquid and solid-state electrolytes, particularly under fast charging conditions. First, the lithium metal growth behavior in liquid electrolytes was discussed in terms of mass transport and charge transport kinetics. We also demonstrated various strategies for enhancing fast charging kinetics in LMBs, including (i) regulating bulk electrolyte pathways, (ii) homogenizing lithium-ion flux at the electrode/electrolyte interface, (iii)

introducing a 3D porous framework electrode structure, and (iv) developing advanced electrolytes. Then, we discussed the lithium growth behavior for solid-state electrolytes and the relevant strategies suppressing lithium dendrites, focusing on (i) the electrolyte/electrode interfacial characteristics, (ii) void formation and contact loss during repeated cycling, (iii) chemical/electrochemical stability at the interface between solid electrolyte and lithium metal, and (iv) introducing a modified solid electrolyte structure. The electrochemical performances of LMBs with liquid and solid electrolytes under fast charging conditions are summarized in Figure 7a and b, respectively. Detailed strategies and operating conditions are also presented in Table 2 and Table 3, respectively. To ensure a direct comparison of lithium metal performance solely under fast charging conditions, this summary focuses on literature reporting charging rates of 5 mA cm^{-2} or higher in liquid electrolytes and 0.5 mA cm^{-2} or higher in solid-state electrolytes. This comparison shows the current status of lithium metal batteries with liquid and solid electrolytes regarding fast charging performance. The fast charging performance of lithium metal batteries with liquid electrolytes has been effectively enhanced through the implementation of various successful strategies. However, they often overlook the decreases in the volumetric and gravimetric energy densities of LMBs when enhancing the rate performance of LMBs. As both fast charging performance and high energy density have become essential, it will be crucial to strike a proper balance between the two factors when constructing advanced lithium metal batteries.

Moreover, most previous literature investigated the failure mechanism of lithium metal using microscopic analysis tools to observe the dendrite growth behavior of lithium metal in nanoscale and microscale. However, Figure 8 shows operando spatial pressure mapping analysis images at various C rates for large scale pressurized Li | NMC811 pouch cells ($5 \times 5 \text{ cm}^2$). Macroscopically inhomogeneous deposition and dissolution of lithium metal were identified as a primary cause of the abrupt capacity fading of the large cell during fast charging conditions. For this reason, the key to enhancing the fast charging performance of LMBs in the future lies in the regulation of macroscopic homogeneous lithium plating and stripping.

In addition, although ASSLMBs have shown promises in improved electrochemical performance, they still face more significant challenges compared to LMBs with liquid electrolytes, particularly at high current densities. To enhance the fast charging performance of ASSLMBs, a more comprehensive understanding of the lithium dendrite growth mechanism for solid-state electrolytes is required. Moreover, cell configuration, separator thickness, and the optimal pressure and temperature conditions were far from the practical conditions of prototype ASSLMBs, during the evaluation of the cell performance of ASSLMBs. This made it difficult to fairly compare various strategies for improving the electrochemical performance of ASSLMBs. Therefore, there is a demand to standardize the cell fabrication and evaluation conditions. This review provides a comprehensive understanding of the critical factors determining the electrochemical performances of lithium metal electro-

des with liquid and solid electrolytes under fast charging conditions. It also offers insights into the realization of fast charging lithium metal batteries for both liquid and solid electrolytes.

Acknowledgements

K.P and J.S contributed equally to this work. This work was supported by the Hyundai Motor Company and National Research Foundation of Korea (NRF) grant funded by the Korea government (MSIT) (2020M3H4A1A03082971, 2018R1A5A1024127, and 2022M3H4A6A01037200).

Conflict of Interests

The authors declare no conflict of interest.

Keywords: fast charging • lithium metal anode • solid-state electrolyte • liquid electrolyte • batteries

- [1] Y. Liu, Y. Zhu, Y. Cui, *Nat. Energy* **2019**, *4*, 540.
- [2] R. Collin, Y. Miao, A. Yokochi, P. Enjeti, A. V. Jouanne, *Energies* **2019**, *12*, 1839.
- [3] J. Janek, W. G. Zeier, *Nat. Energy* **2016**, *1*, 16141.
- [4] W. Xu, J. Wang, F. Ding, X. Chen, E. Nasibulin, Y. Zhang, J.-G. Zhang, *Energy Environ. Sci.* **2014**, *7*, 513.
- [5] E. R. Logan, J. R. Dahn, *Trends Chem.* **2020**, *2*, 354.
- [6] P. Albertus, S. Babinec, S. Litzman, A. Newman, *Nat. Energy* **2018**, *3*, 16.
- [7] Z. Lin, T. Liu, X. Ai, C. Liang, *Nat. Commun.* **2018**, *9*, 5262.
- [8] C.-Y. Wang, T. Liu, X.-G. Yang, S. Ge, N. V. Stanley, E. S. Rountree, Y. Leng, B. D. McCarthy, *Nature* **2022**, *611*, 485.
- [9] X.-B. Cheng, R. Zhang, C.-Z. Zhao, Q. Zhang, *Chem. Rev.* **2017**, *117*, 10403.
- [10] Y. Takeda, O. Yamamoto, N. Imanishi, *Electrochim. Acta* **2016**, *84*, 210.
- [11] K. Park, M. Lee, J. Song, A. R. Ha, S. Ha, S. Jo, J. Song, S. H. Choi, W. Kim, K. Ryu, J. Nam, K. T. Lee, *Adv. Sci.* **2023**, 2304979.
- [12] H. Wu, H. Jia, C. Wang, J.-G. Zhang, W. Xu, *Adv. Energy Mater.* **2021**, *11*, 2003092.
- [13] G. Li, *Adv. Energy Mater.* **2021**, *11*, 2002891.
- [14] A. Manthiram, X. Yu, S. Wang, *Nat. Rev. Mater.* **2017**, *2*, 16103.
- [15] J. C. Bachman, S. Muy, A. Grimaud, H.-H. Chang, N. Pour, S. F. Lux, O. Paschos, F. Maglia, S. Lupart, P. Lamp, L. Giordano, Y. Shao-Horn, *Chem. Rev.* **2016**, *116*, 140.
- [16] C. Heubner, S. Maletti, H. Auer, J. Hüttl, K. Voigt, O. Lohrberg, K. Niklowski, M. Partsch, A. Michaelis, *Adv. Funct. Mater.* **2021**, *31*, 2106608.
- [17] A. J. Louli, A. Eladesoky, R. Weber, M. Genovese, M. Coon, J. deGooyer, Z. Deng, R. T. White, J. Lee, T. Rodgers, R. Petibon, S. Hy, S. J. H. Cheng, J. R. Dahn, *Nat. Energy* **2020**, *5*, 693.
- [18] T. Krauskopf, F. H. Richter, W. G. Zeier, J. Janek, *Chem. Rev.* **2020**, *120*, 7745.
- [19] P. Wang, W. Qu, W.-L. Song, H. Chen, R. Chen, D. Fang, *Adv. Funct. Mater.* **2019**, *29*, 1900950.
- [20] A. Mauger, M. Armand, C. M. Julien, K. Zaghib, *J. Power Sources* **2017**, *353*, 333.
- [21] S. Xia, X. Wu, Z. Zhang, Y. Cui, W. Liu, *Chem* **2019**, *5*, 753.
- [22] P. Bai, J. Li, F. R. Brushett, M. Z. Bazant, *Energy Environ. Sci.* **2016**, *9*, 3221.
- [23] P. Zhou, X. Zhang, Y. Xiang, K. Liu, *Nano Res.* **2023**, *16*, 8055.
- [24] K. M. Diederichsen, E. J. McShane, B. D. McCloskey, *ACS Energy Lett.* **2017**, *2*, 2563.
- [25] H. Yang, L. Yin, H. Shi, K. He, H.-M. Cheng, F. Li, *Chem. Commun.* **2019**, *55*, 13211.

- [26] S. Jo, B. Kwon, J. Oh, J. Lee, K. Park, K. T. Lee, *J. Mater. Chem. A* **2022**, *10*, 5520.
- [27] Y.-Y. Wang, J.-K. Gu, B.-H. Zhang, G.-R. Li, S. Liu, X.-P. Gao, *Adv. Funct. Mater.* **2022**, *32*, 2112005.
- [28] J. Wu, *Chem. Rev.* **2022**, *122*, 10821.
- [29] C. Yan, H.-R. Li, X. Chen, X.-Q. Zhang, X.-B. Cheng, R. Xu, J.-Q. Huang, Q. Zhang, *J. Am. Chem. Soc.* **2019**, *141*, 9422.
- [30] Y. Chen, X. Xu, L. Gao, G. Yu, O. O. Kapitanova, S. Xiong, V. S. Volkov, Z. Song, Y. Liu, *Small* **2022**, *6*, 2200113.
- [31] K. Park, M. Lee, D.-M. Kim, B. Kwon, J. Lee, S. Jo, J. Nam, K. T. Lee, *Adv. Mater. Interfaces* **2021**, *8*, 2100687.
- [32] Z. Hao, Q. Zhang, X. Xu, Q. Zhao, C. Wu, J. Liu, H. Wang, *Nanoscale* **2020**, *12*, 15923.
- [33] Z. Hao, C. Wang, Y. Wu, Q. Zhang, H. Xu, Y. Jin, J. Liu, H. Wang, X. He, *Adv. Energy Mater.* **2023**, *n/a*, 2204007.
- [34] Y. Guo, Q. Wu, L. Liu, G. Li, L. Yang, X. Wang, Y. Ma, Z. Hu, *Adv. Sci.* **2022**, *9*, 2200411.
- [35] A. Jung, M. J. Lee, S. W. Lee, J. Cho, J. G. Son, B. Yeom, *Small* **2022**, *18*, 2205355.
- [36] A. Huang, H. Liu, O. Manor, P. Liu, J. Friend, *Adv. Mater.* **2020**, *32*, 1907516.
- [37] L. Fan, H. L. Zhuang, L. Gao, Y. Lu, L. A. Archer, *J. Mater. Chem. A* **2017**, *5*, 3483.
- [38] Z. Cao, H. Chen, Z. Du, J. Gu, Q. Zhu, B. Li, S. Yang, *Adv. Energy Mater.* **2022**, *12*, 2201189.
- [39] L. Ye, M. Liao, X. Cheng, X. Zhou, Y. Zhao, Y. Yang, C. Tang, H. Sun, Y. Gao, B. Wang, H. Peng, *Angew. Chem. Int. Ed.* **2021**, *60*, 17419.
- [40] A. Hu, W. Chen, X. Du, Y. Hu, T. Lei, H. Wang, L. Xue, Y. Li, H. Sun, Y. Yan, J. Long, C. Shu, J. Zhu, B. Li, X. Wang, J. Xiong, *Energy Environ. Sci.* **2021**, *14*, 4115.
- [41] Z. Liu, Y. Qi, Y. X. Lin, L. Chen, P. Lu, L. Q. Chen, *J. Electrochem. Soc.* **2016**, *163*, A592.
- [42] A. Turak, *Electron. Mater.* **2021**, *2*, 198.
- [43] Z. Wu, C. Wang, Z. Hui, H. Liu, S. Wang, S. Yu, X. Xing, J. Holoubek, Q. Miao, H. L. Xin, P. Liu, *Nat. Energy* **2023**, *8*, 340.
- [44] D. Lin, Y. Liu, W. Chen, G. Zhou, K. Liu, B. Dunn, Y. Cui, *Nano Lett.* **2017**, *17*, 3731.
- [45] F. Hao, A. Verma, P. P. Mukherjee, *ACS Appl. Mater. Interfaces* **2018**, *10*, 26320.
- [46] J. Xiao, *Science* **2019**, *366*, 426.
- [47] H. Sano, H. Sakaebe, H. Senoh, H. Matsumoto, *J. Electrochem. Soc.* **2014**, *161*, A1236.
- [48] E. Santos, W. Schmickler, *Angew. Chem. Int. Ed.* **2021**, *60*, 5876.
- [49] Y. Xu, H. Wu, H. Jia, J.-G. Zhang, W. Xu, C. Wang, *ACS Nano* **2020**, *14*, 8766.
- [50] J. Lee, E.-S. Won, D.-M. Kim, H. Kim, B. Kwon, K. Park, S. Jo, S. Lee, J.-W. Lee, K. T. Lee, *ACS Appl. Mater. Interfaces* **2021**, *13*, 33056.
- [51] C. Niu, H. Pan, W. Xu, J. Xiao, J.-G. Zhang, L. Luo, C. Wang, D. Mei, J. Meng, X. Wang, Z. Liu, L. Mai, J. Liu, *Nat. Nanotechnol.* **2019**, *14*, 594.
- [52] S.-H. Hong, D.-H. Jung, J.-H. Kim, Y.-H. Lee, S.-J. Cho, S. H. Joo, H.-W. Lee, K.-S. Lee, S.-Y. Lee, *Adv. Funct. Mater.* **2020**, *30*, 1908868.
- [53] S. H. Choi, Y. Hyeon, H. R. Shin, G. H. Eom, H. Thi Thu Pham, D. Whang, S. Y. Kim, J.-W. Lee, J. H. Kim, M.-S. Park, *Nano Energy* **2021**, *88*, 106243.
- [54] H. Gong, Y. Chen, S. Chen, C. Xu, Y. Yang, Y. Ye, Z. Huang, R. Ning, Y. Cui, Z. Bao, *ACS Energy Lett.* **2022**, *7*, 4417.
- [55] J.-Y. Song, J. Yoon, J. Suk, M. Wu, H.-T. Jung, *J. Mater. Chem. A* **2023**, *11*, 16153.
- [56] D. W. Kang, S. S. Park, H. J. Choi, J.-H. Park, J. H. Lee, S.-M. Lee, J.-H. Choi, J. Moon, B. G. Kim, *ACS Nano* **2022**, *16*, 11892.
- [57] Y. Fang, S. L. Zhang, Z.-P. Wu, D. Luan, X. W. Lou, *Sci. Adv.* **2021**, *7*, eabg3626.
- [58] J. B. Park, C. Choi, S. Yu, K. Y. Chung, D.-W. Kim, *Adv. Energy Mater.* **2021**, *11*, 2101544.
- [59] G. Yang, I. N. Ivanov, R. E. Ruther, R. L. Sacci, V. Subjakova, D. T. Hallinan, J. Nanda, *ACS Nano* **2018**, *12*, 10159.
- [60] X. Ren, P. Gao, L. Zou, S. Jiao, X. Cao, X. Zhang, H. Jia, M. H. Engelhard, B. E. Matthews, H. Wu, H. Lee, C. Niu, C. Wang, B. W. Arey, J. Xiao, J. Liu, J.-G. Zhang, W. Xu, *PNAS* **2020**, *117*, 28603.
- [61] Z. Jiang, J. Mo, C. Li, H.-W. Li, Q. Zhang, Z. Zeng, J. Xie, Y. Li, *Energy Environ. Mater.* **2022**, *0*, e12440.
- [62] T. D. Pham, A. Bin Faheem, J. Kim, H. M. Oh, K.-K. Lee, *Small* **2022**, *18*, 2107492.
- [63] K. Park, D.-M. Kim, K.-H. Ha, B. Kwon, J. Lee, S. Jo, X. Ji, K. T. Lee, *Adv. Sci.* **2022**, *9*, 2203443.
- [64] S. Ko, T. Obukata, T. Shimada, N. Takenaka, M. Nakayama, A. Yamada, Y. Yamada, *Nat. Energy* **2022**, *7*, 1217.
- [65] S. C. Kim, X. Kong, R. A. Vilá, W. Huang, Y. Chen, D. T. Boyle, Z. Yu, H. Wang, Z. Bao, J. Qin, Y. Cui, *J. Am. Chem. Soc.* **2021**, *143*, 10301.
- [66] D. T. Boyle, S. C. Kim, S. T. Oyakhire, R. A. Vilá, Z. Huang, P. Sayavong, J. Qin, Z. Bao, Y. Cui, *J. Am. Chem. Soc.* **2022**, *144*, 20717.
- [67] S. Angarita-Gomez, P. B. Balbuena, *Mater Adv* **2022**, *3*, 6352.
- [68] J. Qian, W. A. Henderson, W. Xu, P. Bhattacharya, M. Engelhard, O. Borodin, J.-G. Zhang, *Nat. Commun.* **2015**, *6*, 6362.
- [69] L. Dong, Y. Liu, K. Wen, D. Chen, D. Rao, J. Liu, B. Yuan, Y. Dong, Z. Wu, Y. Liang, M. Yang, J. Ma, C. Yang, C. Xia, B. Xia, J. Han, G. Wang, Z. Guo, W. He, *Adv. Sci.* **2022**, *9*, 2104699.
- [70] Z. Yu, H. Wang, X. Kong, W. Huang, Y. Tsao, D. G. Mackanic, K. Wang, X. Wang, W. Huang, S. Choudhury, Y. Zheng, C. V. Amanchukwu, S. T. Hung, Y. Ma, E. G. Lomeli, J. Qin, Y. Cui, Z. Bao, *Nat. Energy* **2020**, *5*, 526.
- [71] J. Holoubek, H. Liu, Z. Wu, Y. Yin, X. Xing, G. Cai, S. Yu, H. Zhou, T. A. Pascal, Z. Chen, P. Liu, *Nat. Energy* **2021**, *6*, 303.
- [72] Z. Yu, P. E. Rudnicki, Z. Zhang, Z. Huang, H. Celik, S. T. Oyakhire, Y. Chen, X. Kong, S. C. Kim, X. Xiao, H. Wang, Y. Zheng, G. A. Kamat, M. S. Kim, S. F. Bent, J. Qin, Y. Cui, Z. Bao, *Nat. Energy* **2022**, *7*, 94.
- [73] Y. Zhao, T. Zhou, M. Mensi, J. W. Choi, A. Coskun, *Nat. Commun.* **2023**, *14*, 299.
- [74] Y. Zhao, T. Zhou, T. Ashirov, M. E. Kazzi, C. Cancellieri, L. P. H. Jeurgens, J. W. Choi, A. Coskun, *Nat. Commun.* **2022**, *13*, 2575.
- [75] W. Xue, Z. Shi, M. Huang, S. Feng, C. Wang, F. Wang, J. Lopez, B. Qiao, G. Xu, W. Zhang, Y. Dong, R. Gao, Y. Shao-Horn, J. A. Johnson, J. Li, *Energy Environ. Sci.* **2020**, *13*, 212.
- [76] W. Xue, M. Huang, Y. Li, Y. G. Zhu, R. Gao, X. Xiao, W. Zhang, S. Li, G. Xu, Y. Yu, P. Li, J. Lopez, D. Yu, Y. Dong, W. Fan, Z. Shi, R. Xiong, C.-J. Sun, I. Hwang, W.-K. Lee, Y. Shao-Horn, J. A. Johnson, J. Li, *Nat. Energy* **2021**, *6*, 495.
- [77] M. Wu, Z. Wang, W. Zhang, C. Jayawardana, Y. Li, F. Chen, B. Nan, B. L. Lucht, C. Wang, *Angew. Chem. Int. Ed.* **2023**, *62*, e202216169.
- [78] G. Zhang, J. Chang, L. Wang, J. Li, C. Wang, R. Wang, G. Shi, K. Yu, W. Huang, H. Zheng, T. Wu, Y. Deng, J. Lu, *Nat. Commun.* **2023**, *14*, 1081.
- [79] X. Cao, P. Gao, X. Ren, L. Zou, M. H. Engelhard, B. E. Matthews, J. Hu, C. Niu, D. Liu, B. W. Arey, C. Wang, J. Xiao, J. Liu, W. Xu, J.-G. Zhang, *PNAS* **2021**, *118*, e2020357118.
- [80] S. Kim, S. O. Park, M.-Y. Lee, J.-A. Lee, I. Kristanto, T. K. Lee, D. Hwang, J. Kim, T.-U. Wi, H.-W. Lee, S. K. Kwak, N.-S. Choi, *Energy Storage Mater.* **2022**, *45*, 1.
- [81] B. Flamme, G. Rodriguez Garcia, M. Weil, M. Haddad, P. Phansavath, V. Ratovelomanana-Vidal, A. Chagnes, *Green Chem.* **2017**, *19*, 1828.
- [82] R. Schmuck, R. Wagner, G. Höppl, T. Placke, M. Winter, *Nat. Energy* **2018**, *3*, 267.
- [83] L. Ye, Y. Li, *Nature* **2021**, *593*, 218.
- [84] T. Kim, K. Kim, S. Lee, G. Song, M. S. Jung, K. T. Lee, *Chem. Mater.* **2022**, *34*, 9159.
- [85] T. Krauskopf, B. Mogwitz, H. Hartmann, D. K. Singh, W. G. Zeier, J. Janek, *Adv. Energy Mater.* **2020**, *10*, 2000945.
- [86] M. Chiku, W. Tsujiwaki, E. Higuchi, H. Inoue, *J. Power Sources* **2013**, *244*, 675.
- [87] Y. Lu, C.-Z. Zhao, H. Yuan, X.-B. Cheng, J.-Q. Huang, Q. Zhang, *Adv. Funct. Mater.* **2021**, *31*, 2009925.
- [88] S. Sarkar, V. Thangadurai, *ACS Energy Lett.* **2022**, *7*, 1492.
- [89] L. Cheng, W. Chen, M. Kunz, K. Persson, N. Tamura, G. Chen, M. Doeff, *ACS Appl. Mater. Interfaces* **2015**, *7*, 2073.
- [90] T. Swamy, R. Park, B. W. Sheldon, D. Rettenwander, L. Porz, S. Berendts, R. Uecker, W. C. Carter, Y.-M. Chiang, *J. Electrochem. Soc.* **2018**, *165*, A3648.
- [91] Z. Ning, G. Li, D. L. R. Melvin, Y. Chen, J. Bu, D. Spencer-Jolly, J. Liu, B. Hu, X. Gao, J. Perera, C. Gong, S. D. Pu, S. Zhang, B. Liu, G. O. Hartley, A. J. Bodey, R. I. Todd, P. S. Grant, D. E. J. Armstrong, T. J. Marrow, C. W. Monroe, P. G. Bruce, *Nature* **2023**, *618*, 287.
- [92] T. Krauskopf, H. Hartmann, W. G. Zeier, J. Janek, *ACS Appl. Mater. Interfaces* **2019**, *11*, 14463.
- [93] J. A. Lewis, F. J. Q. Cortes, M. G. Boebinger, J. Tippens, T. S. Marchese, N. Kondekar, X. Liu, M. Chi, M. T. McDowell, *ACS Energy Lett.* **2019**, *4*, 591.
- [94] W. Manalastas, J. Rikarte, R. J. Chater, R. Brugge, A. Aguadero, L. Buannic, A. Llordés, F. Aguesse, J. Kilner, *J. Power Sources* **2019**, *412*, 287.
- [95] Y. Song, L. Yang, W. Zhao, Z. Wang, Y. Zhao, Z. Wang, Q. Zhao, H. Liu, F. Pan, *Adv. Energy Mater.* **2019**, *9*, 1900671.

- [96] B. Xu, W. Li, H. Duan, H. Wang, Y. Guo, H. Li, H. Liu, *J. Power Sources* **2017**, *354*, 68.
- [97] J. Janek, W. G. Zeier, *Nat. Energy* **2023**, *8*, 230.
- [98] Y. Wu, S. Wang, H. Li, L. Chen, F. Wu, *InfoMat* **2021**, *3*, 827.
- [99] Y. Nikodimos, C.-J. Huang, B. W. Taklu, W.-N. Su, B. J. Hwang, *Energy Environ. Sci.* **2022**, *15*, 991.
- [100] Y. Nikodimos, W.-N. Su, B. J. Hwang, *Adv. Energy Mater.* **2023**, *13*, 2202854.
- [101] C. F. N. Marchiori, R. P. Carvalho, M. Ebadi, D. Brandell, C. M. Araujo, *Chem. Mater.* **2020**, *32*, 7237.
- [102] M. R. Bin Mamta, X. Michaud, H. Jo, S. S. Park, *Int. J. Precis. Eng. Manuf. - Green Technol.* **2023**, *10*, 1093.
- [103] K. Kim, D. Park, H.-G. Jung, K. Y. Chung, J. H. Shim, B. C. Wood, S. Yu, *Chem. Mater.* **2021**, *33*, 3669.
- [104] D. Karabelli, K. P. Birke, M. Weeber, *Batteries* **2021**, *7*, 18.
- [105] Y. Lu, X. Huang, Z. Song, K. Rui, Q. Wang, S. Gu, J. Yang, T. Xiu, M. E. Badding, Z. Wen, *Energy Storage Mater.* **2018**, *15*, 282.
- [106] J. Kasemchainan, S. Zekoll, D. Spencer Jolly, Z. Ning, G. O. Hartley, J. Marrow, P. G. Bruce, *Nat. Mater.* **2019**, *18*, 1105.
- [107] G. Bucci, J. Christensen, *J. Power Sources* **2019**, *441*, 227186.
- [108] Y. C. Chen, C. Y. Ouyang, L. J. Song, Z. L. Sun, *J. Phys. Chem. C* **2011**, *115*, 7044.
- [109] S. Lee, K.-s. Lee, S. Kim, K. Yoon, S. Han, M. H. Lee, Y. Ko, J. H. Noh, W. Kim, K. Kang, *Sci. Adv.* **2022**, *8*, eabq0153.
- [110] J. Su, M. Pasta, Z. Ning, X. Gao, P. G. Bruce, C. R. M. Grovenor, *Energy Environ. Sci.* **2022**, *15*, 3805.
- [111] B. Li, Z. Sun, N. Lv, Y. Hu, L. Jiang, Z. Zhang, F. Liu, *ACS Appl. Mater. Interfaces* **2022**, *14*, 37738.
- [112] H. J. Choi, D. W. Kang, J.-W. Park, J.-H. Park, Y.-J. Lee, Y.-C. Ha, S.-M. Lee, S. Y. Yoon, B. G. Kim, *Adv. Sci.* **2022**, *9*, 2103826.
- [113] Y.-G. Lee, S. Fujiki, C. Jung, N. Suzuki, N. Yashiro, R. Omoda, D.-S. Ko, T. Shiratsuchi, T. Sugimoto, S. Ryu, J. H. Ku, T. Watanabe, Y. Park, Y. Aihara, D. Im, I. T. Han, *Nat. Energy* **2020**, *5*, 299.
- [114] Y. Zhu, X. He, Y. Mo, *ACS Appl. Mater. Interfaces* **2015**, *7*, 23685.
- [115] S. Wenzel, S. Randau, T. Leichtweiss, D. A. Weber, J. Sann, W. G. Zeier, J. Janek, *Chem. Mater.* **2016**, *28*, 2400.
- [116] S. Wenzel, T. Leichtweiss, D. Krüger, J. Sann, J. Janek, *Solid State Ionics* **2015**, *278*, 98.
- [117] Y. Su, L. Ye, W. Fitzhugh, Y. Wang, E. Gil-González, I. Kim, X. Li, *Energy Environ. Sci.* **2020**, *13*, 908.
- [118] B. W. Taklu, Y. Nikodimos, H. K. Bezabh, K. Lakshmanan, T. M. Hagos, T. A. Nigatu, S. K. Merso, H.-Y. Sung, S.-C. Yang, S.-H. Wu, W.-N. Su, B. J. Hwang, *Nano Energy* **2023**, *112*, 108471.
- [119] F. Zhao, Q. Sun, C. Yu, S. Zhang, K. Adair, S. Wang, Y. Liu, Y. Zhao, J. Liang, C. Wang, X. Li, X. Li, W. Xia, R. Li, H. Huang, L. Zhang, S. Zhao, S. Lu, X. Sun, *ACS Energy Lett.* **2020**, *5*, 1035.
- [120] C. Liu, B. Chen, T. Zhang, J. Zhang, R. Wang, J. Zheng, Q. Mao, X. Liu, *Angew. Chem. Int. Ed.* **2023**, *62*, e202302655.
- [121] K. Kim, T. Kim, G. Song, S. Lee, M. S. Jung, S. Ha, A. R. Ha, K. T. Lee, *Adv. Sci.* **2023**, *2303308*.
- [122] G. T. Hitz, D. W. McOwen, L. Zhang, Z. Ma, Z. Fu, Y. Wen, Y. Gong, J. Dai, T. R. Hamann, L. Hu, E. D. Wachsman, *Mater. Today* **2019**, *22*, 50.
- [123] H. Xie, C. Yang, Y. Ren, S. Xu, T. R. Hamann, D. W. McOwen, E. D. Wachsman, L. Hu, *Nano Lett.* **2021**, *21*, 6163.
- [124] G. V. Alexander, C. Shi, J. O'Neill, E. D. Wachsman, *Nat. Mater.* **2023**, *22*, 1136.
- [125] R. Xu, F. Liu, Y. Ye, H. Chen, R. R. Yang, Y. Ma, W. Huang, J. Wan, Y. Cui, *Adv. Mater.* **2021**, *33*, 2104009.
- [126] X. Shen, Y. Li, T. Qian, J. Liu, J. Zhou, C. Yan, J. B. Goodenough, *Nat. Commun.* **2019**, *10*, 900.
- [127] H. Kim, Y. S. Kim, J. Yoo, *Sustain. Energy Fuels* **2020**, *4*, 522.
- [128] S. Xia, X. Zhang, C. Liang, Y. Yu, W. Liu, *Energy Storage Mater.* **2020**, *24*, 329.
- [129] S. Li, L. Fan, Y. Lu, *Energy Storage Mater.* **2019**, *18*, 205.
- [130] X. Chen, M. Shang, J. Niu, *Nano Lett.* **2020**, *20*, 2639.
- [131] Z. Lu, W. Li, Y. Long, J. Liang, Q. Liang, S. Wu, Y. Tao, Z. Weng, W. Lv, Q.-H. Yang, *Adv. Funct. Mater.* **2020**, *30*, 1907343.
- [132] G. Wang, C. Chen, Y. Chen, X. Kang, C. Yang, F. Wang, Y. Liu, X. Xiong, *Angew. Chem. Int. Ed.* **2020**, *59*, 2055.
- [133] T. Liu, Q. Hu, X. Li, L. Tan, G. Yan, Z. Wang, H. Guo, Y. Liu, Y. Wu, J. Wang, *J. Mater. Chem. A* **2019**, *7*, 20911.
- [134] F. Zhao, W. Deng, D. Dong, X. Zhou, Z. Liu, *Mater. Today Energy* **2022**, *26*, 100988.
- [135] B. Xu, Z. Liu, J. Li, X. Huang, B. Qie, T. Gong, L. Tan, X. Yang, D. Paley, M. Dontigny, K. Zaghib, X. Liao, Q. Cheng, H. Zhai, X. Chen, L.-Q. Chen, C.-W. Nan, Y.-H. Lin, Y. Yang, *Nano Energy* **2020**, *67*, 104242.
- [136] P. Zhao, Y. Feng, T. Li, B. Li, L. Hu, K. Sun, C. Bao, S. Xiong, A. Matic, J. Song, *Energy Storage Mater.* **2020**, *33*, 158.
- [137] C. Yan, X.-B. Cheng, Y. Tian, X. Chen, X.-Q. Zhang, W.-J. Li, J.-Q. Huang, Q. Zhang, *Adv. Mater.* **2018**, *30*, 1707629.
- [138] K. Huang, Z. Li, Q. Xu, H. Liu, H. Li, Y. Wang, *Adv. Energy Mater.* **2019**, *9*, 1900853.
- [139] Y. Liao, L. Yuan, J. Xiang, W. Zhang, Z. Cheng, B. He, Z. Li, Y. Huang, *Nano Energy* **2020**, *69*, 104471.
- [140] S. Li, Q. Liu, J. Zhou, T. Pan, L. Gao, W. Zhang, L. Fan, Y. Lu, *Adv. Funct. Mater.* **2019**, *29*, 1808847.
- [141] G. Huang, J. Han, F. Zhang, Z. Wang, H. Kashani, K. Watanabe, M. Chen, *Adv. Mater.* **2019**, *31*, 1805334.
- [142] L. Dong, L. Nie, W. Liu, *Adv. Mater.* **2020**, *32*, 1908494.
- [143] Q. Zhao, X. Hao, S. Su, J. Ma, Y. Hu, Y. Liu, F. Kang, Y.-B. He, *J. Mater. Chem. A* **2019**, *7*, 15871.
- [144] H. Wang, D. Lin, J. Xie, Y. Liu, H. Chen, Y. Li, J. Xu, G. Zhou, Z. Zhang, A. Pei, Y. Zhu, K. Liu, K. Wang, Y. Cui, *Adv. Energy Mater.* **2019**, *9*, 1802720.
- [145] J. Xie, J. Ye, F. Pan, X. Sun, K. Ni, H. Yuan, X. Wang, N. Shu, C. Chen, Y. Zhu, *Adv. Mater.* **2019**, *31*, 1805654.
- [146] H. Shi, M. Yue, C. J. Zhang, Y. Dong, P. Lu, S. Zheng, H. Huang, J. Chen, P. Wen, Z. Xu, Q. Zheng, X. Li, Y. Yu, Z.-S. Wu, *ACS Nano* **2020**, *14*, 8678.
- [147] H. Shi, C. J. Zhang, P. Lu, Y. Dong, P. Wen, Z.-S. Wu, *ACS Nano* **2019**, *13*, 14308.
- [148] Z. Lyu, G. J. H. Lim, R. Guo, Z. Pan, X. Zhang, H. Zhang, Z. He, S. Adams, W. Chen, J. Ding, J. Wang, *Energy Storage Mater.* **2020**, *24*, 336.
- [149] H. Xu, S. Li, X. Chen, C. Zhang, Z. Tang, H. Fan, Y. Yu, W. Liu, N. Liang, Y. Huang, J. Li, *Nano Energy* **2020**, *74*, 104815.
- [150] X. Gao, X. Yang, K. Adair, X. Li, J. Liang, Q. Sun, Y. Zhao, R. Li, T.-K. Sham, X. Sun, *Adv. Energy Mater.* **2020**, *10*, 1903753.
- [151] H. Wang, D. Lin, Y. Liu, Y. Li, Y. Cui, *Sci. Adv.* **2017**, *3*, e1701301.
- [152] S. Liu, X. Ji, J. Yue, S. Hou, P. Wang, C. Cui, J. Chen, B. Shao, J. Li, F. Han, J. Tu, C. Wang, *J. Am. Chem. Soc.* **2020**, *142*, 2438.
- [153] D. Zhang, R. Gu, W. Guo, Q. Xu, H. Li, Y. Min, *ACS Appl. Mater. Interfaces* **2021**, *13*, 60678.
- [154] C. Chen, Q. Liang, G. Wang, D. Liu, X. Xiong, *Adv. Funct. Mater.* **2022**, *32*, 2107249.
- [155] D. Zhu, J. Xu, K. Ding, Q. Xu, P. Shi, Y. Min, *Adv. Funct. Mater.* **2023**, *33*, 2213822.
- [156] K. Lee, S. Han, J. Lee, S. Lee, J. Kim, Y. Ko, S. Kim, K. Yoon, J.-H. Song, J. H. Noh, K. Kang, *ACS Energy Lett.* **2022**, *7*, 381.
- [157] C. Zheng, Y. Lu, Q. Chang, Z. Song, T. Xiu, J. Jin, M. E. Badding, Z. Wen, *Adv. Funct. Mater.* **2023**, 2302729.
- [158] J. Cui, J. H. Kim, S. Yao, A. Guerfi, A. Paolella, J. B. Goodenough, H. Khan, *Adv. Funct. Mater.* **2023**, *33*, 2210192.
- [159] H. Su, Y. Liu, Y. Zhong, J. Li, X. Wang, X. Xia, C. Gu, J. Tu, *Nano Energy* **2022**, *96*, 107104.
- [160] B. Pang, Z. Wu, W. Zhang, H. Huang, Y. Gan, Y. Xia, X. He, X. Xia, J. Zhang, *J. Power Sources* **2023**, *563*, 232836.
- [161] Y. Tian, Y. Zhou, W. Wang, Y. Zhou, *J. Alloys Compd.* **2023**, *950*, 169942.
- [162] L. Zhai, K. Yang, F. Jiang, W. Liu, Z. Yan, J. Sun, *J. Energy Chem.* **2023**, *79*, 357.
- [163] X. He, S. Hua, F. Yan, H. Bai, B. Shen, J. Zhai, *Chem. Eng. J.* **2021**, *421*, 127727.
- [164] X. He, F. Yan, M. Gao, Y. Shi, G. Ge, B. Shen, J. Zhai, *ACS Appl. Mater. Interfaces* **2021**, *13*, 42212.
- [165] H. Huo, J. Gao, N. Zhao, D. Zhang, N. G. Holmes, X. Li, Y. Sun, J. Fu, R. Li, X. Guo, X. Sun, *Nat. Commun.* **2021**, *12*, 176.
- [166] X. He, X. Ji, B. Zhang, N. D. Rodrigo, S. Hou, K. Gaskell, T. Deng, H. Wan, S. Liu, J. Xu, B. Nan, B. Lucht, C. Wang, *ACS Energy Lett.* **2022**, *7*, 131.
- [167] Z. Wan, K. Shi, Y. Huang, L. Yang, Q. Yun, L. Chen, F. Ren, F. Kang, Y.-B. He, *J. Power Sources* **2021**, *505*, 230062.
- [168] H. Duan, C. Wang, R. Yu, W. Li, J. Fu, X. Yang, X. Lin, M. Zheng, X. Li, S. Deng, X. Hao, R. Li, J. Wang, H. Huang, X. Sun, *Adv. Energy Mater.* **2023**, *13*, 2300815.
- [169] H. Zhang, F. Okur, C. Cancellieri, L. P. H. Jeurgens, A. Parrilli, D. T. Karabay, M. Nesvadba, S. Hwang, A. Neels, M. V. Kovalenko, K. V. Kravchyk, *Adv. Sci.* **2023**, *10*, 2205821.
- [170] Z. Ge, N. Chen, R. Wang, R. Ma, B. Fan, D. Lecoq, X. Zhang, H. Ma, B. Xue, *Chem. Eng. J.* **2023**, *467*, 143409.
- [171] F. Zhao, J. Liang, C. Yu, Q. Sun, X. Li, K. Adair, C. Wang, Y. Zhao, S. Zhang, W. Li, S. Deng, R. Li, Y. Huang, H. Huang, L. Zhang, S. Zhao, S. Lu, X. Sun, *Adv. Energy Mater.* **2020**, *10*, 1903422.

- [172] B. W. Taklu, W.-N. Su, Y. Nikodimos, K. Lakshmanan, N. T. Temesgen, P.-X. Lin, S.-K. Jiang, C.-J. Huang, D.-Y. Wang, H.-S. Sheu, S.-H. Wu, B. J. Hwang, *Nano Energy* **2021**, *90*, 106542.
- [173] Y. Liu, H. Su, M. Li, J. Xiang, X. Wu, Y. Zhong, X. Wang, X. Xia, C. Gu, J. Tu, *J. Mater. Chem. A* **2021**, *9*, 13531.
- [174] N. Ahmad, S. Sun, P. Yu, W. Yang, *Adv. Funct. Mater.* **2022**, *32*, 2201528.
- [175] C. Zheng, J. Su, Z. Song, T. Xiu, J. Jin, M. E. Badding, Z. Wen, *Mater. Today Energy* **2022**, *27*, 101034.
- [176] H. Zheng, S. Wu, R. Tian, Z. Xu, H. Zhu, H. Duan, H. Liu, *Adv. Funct. Mater.* **2020**, *30*, 1906189.

Manuscript received: August 1, 2023

Revised manuscript received: October 15, 2023

Accepted manuscript online: October 16, 2023

Version of record online: November 8, 2023
